

Narrowband Radio Technosignature Search toward 3I/ATLAS with FAST

JIAN-KANG LI ^{1,2} ZHEN-ZHAO TAO ^{3,4} AND TONG-JIE ZHANG  ^{1,2}

¹*Institute for Frontiers in Astronomy and Astrophysics, Beijing Normal University, Beijing 102206, People's Republic of China*

²*School of Physics and Astronomy, Beijing Normal University, Beijing 100875, People's Republic of China; tjzhang@bnu.edu.cn*

³*Institute for Astronomical Science, Dezhou University, Dezhou 253023, People's Republic of China*

⁴*College of Computer and Information, Dezhou University, Dezhou 253023, People's Republic of China*

ABSTRACT

3I/ATLAS is the third confirmed interstellar object passing through the Solar System. In this work, we conduct narrowband radio technosignature search toward 3I/ATLAS using the Five-hundred-meter Aperture Spherical Telescope (FAST) L-band multibeam receiver from October 2025 to January 2026 on 4 separate dates (i.e. Mars closest, perihelion, Earth closest and flew away from Earth, respectively). We carry out frequency-drifting signal searching with signal-to-noise ratio (SNR) over 10 within 1.05-1.45 GHz via `bliss` pipeline. These signal hits are grouping into event by beam, frequency and drift rate matching, the events are then filtered by cluster analysis and drift rate cut-off. We also characterized the events by their significance in SNR, structure tensor as well as principal component analysis (PCA). No credible narrowband radio technosignature are detected from 3I/ATLAS after visual inspections. The null results place constraints on the presence of transmitters above 2.862×10^{-3} W. We further introduce a Bayesian inference framework to constraints on the existence probability and characteristic power of hypothetical transmitters using physically motivated priors to bracket plausible transmitter scenarios.

Keywords: Search for extraterrestrial intelligence (2127); Radio astronomy (1338); Interstellar objects(52); Astrobiology (74)

1. INTRODUCTION

The Search for Extraterrestrial Intelligence (SETI) endeavors to identify potential technosignatures as observable manifestations of technology, without presupposing the physical nature of their sources. Narrowband radio emission has long been recognized as a promising technosignature, motivated by the fact that such emissions are not known to arise from natural astrophysical processes (Tarter 2001) and can be transmitted efficiently with low energy requirements and minimal propagation losses (Cocconi & Morrison 1959).

Historically, radio SETI efforts have overwhelmingly focused on stars and planetary systems, particularly those hosting exoplanets (Sheikh et al. 2020; Traas et al. 2021; Smith et al. 2021; Margot et al. 2021; Tao et al. 2022, 2023; Luan et al. 2025; Li et al. 2026), while small bodies in Solar system such as comets have received little dedicated attention, reflecting their astrophysical relevance as potential long-term sites for technological activity. However, this focus does not imply that other categories of astrophysical objects are excluded from consideration. Rather, SETI search is guided by the detectability of technosignatures, and objects that are uncommon or observationally transient still therefore warrant targeted search.

3I/ATLAS was discovered on 2025 July 1 by the Asteroid Terrestrial-impact Last Alert System (ATLAS) station. As the third confirmed interstellar object (ISO) traverse the Solar System, similar to the previous confirmed ISO 1I/'Oumuamua and 2I/Borisov, 3I/ATLAS follows an unbound hyperbolic trajectory with eccentricity of 6.1394 and perihelion of 1.3564 AU¹. Numerous observations have conformed its cometary activity, including the presence of a coma (Seligman et al. 2025; Bolin et al. 2025b; Farnham et al. 2025), a Sun-facing plume (Opitom et al. 2025; Cordiner et al. 2025; Santana-Ros et al. 2025; Jewitt et al. 2025) and a tail (Kareta et al. 2025; Bolin et al. 2025a). The reported

¹ Orbital elements are taken from JPL Horizons: <https://ssd.jpl.nasa.gov/horizons/>

non-gravitational acceleration also consistent with outgassing-driven forces expected for an active comet (Eubanks et al. 2025; Jewitt et al. 2025; Neukart 2025).

Although the available observational evidence favors a cometary interpretation for 3I/ATLAS, it remains an unusually rare and time-limited target for sensitive radio observations. As the third confirmed interstellar object, it provides a well-defined opportunity to extend narrowband SETI search to a distinct class of nearby transient objects. Several dedicated SETI observations of 3I/ATLAS have already been carried out by Breakthrough Listen utilizing Allen telescope array (Sheikh et al. 2025, ATA), MeerKAT (Pisano et al. 2025) and Green Bank Telescope (Jacobson-Bell et al. 2025, GBT), with analyses reported to date yielding null results.

As the largest single-dish radio telescope in the world, FAST can achieve unprecedented sensitivity for detecting faint signal (Jiang et al. 2019, 2020; Li et al. 2020; Qian et al. 2020). Previous FAST SETI efforts have predominantly targeted extrasolar systems, including nearby stars and globular clusters (Tao et al. 2022, 2023; Huang et al. 2023; Luan et al. 2025; Li et al. 2026; Huang et al. 2026). Besides, FAST has also been used to observe Solar System comets, primarily for molecular line studies (Chen et al. 2024; Jiang et al. 2025).

In this work, we use FAST multibeam L-band observations of 3I/ATLAS obtained at multiple epochs, during which the object’s sky position and observing geometry changed, to carry out a dedicated search for narrowband Doppler-drift radio signals, extending narrowband SETI observations to an interstellar comet during its brief passage through the inner Solar System. We introduce Bayes factor to quantify the significance of the difference in SNR between on-source and off-source. Furthermore, we also utilize structure tensor and PCA to characterize the signals we detect for further analysis. In section 2, we discuss the observation setting in this work. The data analysis and signal characterization are introduced in section 3, and the corresponding results are presented in section 4. Section 5 is the implication of our results and section 6 lists the conclusion of this work.

2. OBSERVATIONS

2.1. Target Information

We divide our total observation time into four dates, corresponding to different sky position and observing geometry, and each scan lasts for 1 hour. The details for each observation are listed in Table 1, and the relative positions of 3I/ATLAS and Earth are illustrated in Figure 1. The four observation dates we selected correspond to different motion states of 3I/ATLAS: Mars closest approach, perihelion, Earth closest approach, and flew away from Earth.

Table 1. Observation Details of 3I/ATLAS in This Work.

Start Time (UTC)	R.A. (J2000.0)	Decl. (J2000.0)	$\langle d \rangle$ (AU)	$\langle \dot{d} \rangle$ (km/s)	$\langle \theta_{\text{SOT}} \rangle$ (°)
2025-10-03 06:00:00	14:21:06.43	-10:37:00.6	2.4913	-6.9589	26.7492
2025-10-29 03:30:00	13:30:19.35	-07:00:16.5	2.3101	-17.7519	12.3551
2025-12-19 21:13:00	10:43:02.16	+07:21:23.5	1.7977	0.9657	108.414
2026-01-05 18:50:00	09:22:32.32	+13:30:16.8	1.9446	29.7860	146.2780

NOTE—The second and third columns list the mean right ascension and declination for each observation, in the J2000 reference frame. $\langle d \rangle$ and $\langle \dot{d} \rangle$ are the mean geocentric distance between observer and target and its corresponding change rate, respective. $\langle \theta_{\text{SOT}} \rangle$ is the mean Sun-Observer-Target apparent Solar elongation angle seen from the observer.

2.2. Strategy

The traditional on-off position-switching strategy is widely used in single-dish radio SETI observations. In this approach, telescope alternates between on the target position (“on”) and nearby reference pointings (“off”). Artificial technosignatures are expected to be present only in the on-source data and statistically absent in the off-source measurements, which provides a practical discriminator against terrestrial radio frequency interference (RFI) and instrumental artifacts (Enriquez et al. 2017).

The 19-beam receiver of FAST enables a closely related, but more time-efficient, discrimination scheme based on simultaneous multibeam coverage. We adopt a multibeam coincidence matching strategy (MBCM) in which the central

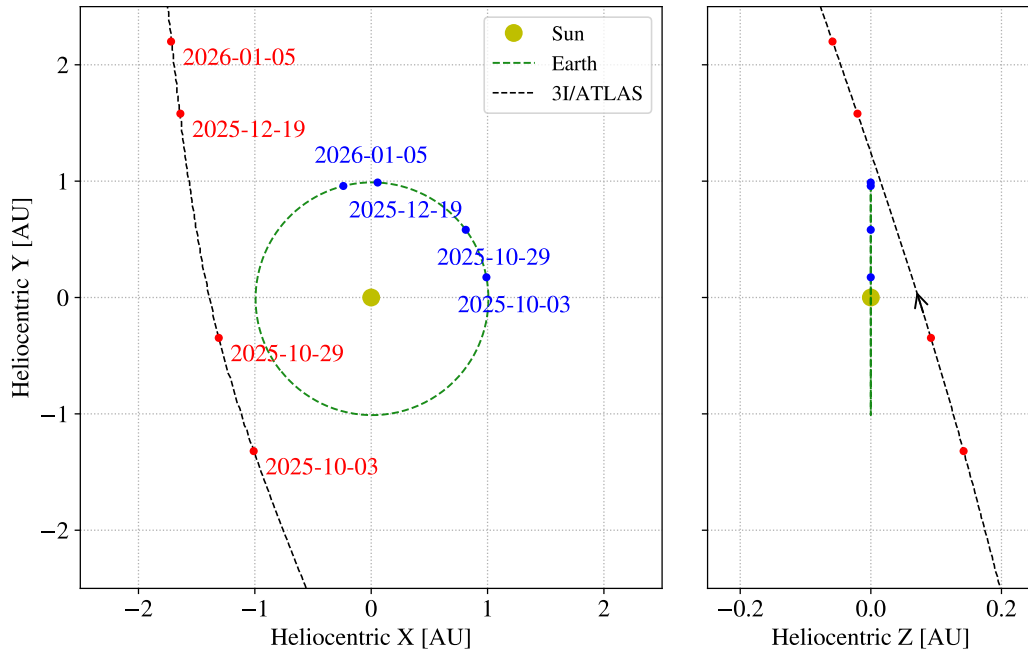


Figure 1. Heliocentric geometry of 3I/ATLAS and the Earth during our observations. The left panel shows the trajectories projected onto the heliocentric ecliptic X-Y plane, while the right panel shows the Z-Y projection.

beam continuously tracks the target as the on-source beam, while other six outermost beams provide contemporaneous reference measurements (See Figure 2). Candidate signals are therefore expected to be confined to the on-source beam and absent in the reference beams, allowing effective rejection of broadband or spatially extended RFI through beam-to-beam consistency checks.

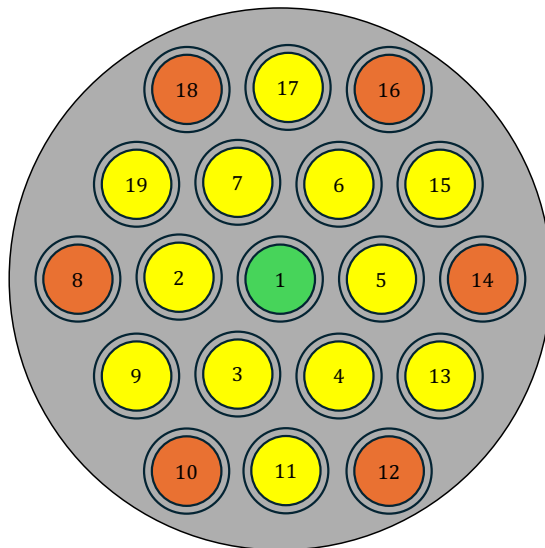


Figure 2. A simple diagram for the multibeam layout of FAST. The central beam is filled with green color, and the six outermost beams filled with orange are the reference beams we use in the search. The angular separation of reference beam is $\sim 11'6$ from the center beam.

2.2.1. FAST Digital Backend

We used the FAST SETI backend, configured with a sampling time of ~ 10 s and a frequency resolution of $\delta\nu = 7.45$ Hz to achieve high spectral resolution. The FAST multibeam digital backend is described in Zhang et al. (2020) and

Li et al. (2020). The data were recorded over 1.0-1.5 GHz with four polarization channels per beam (XX, YY, XY, and YX), corresponding to the auto- and cross-correlations of two orthogonal linear feeds, X and Y. For the analysis we restricted the band to 1.05-1.45 GHz, excluding the outermost 50 MHz at each band edge where the response is degraded by bandpass roll-off. Our narrowband search is performed on all four channels.

3. DATA ANALYSIS

The Doppler-drift search for narrowband signals is performed using `bliss`², a Python package that implements a Taylor-tree-based de-Doppler algorithm. A continuous narrowband signal of extraterrestrial origin is expected to exhibit an apparent frequency drift, $\dot{\nu} \equiv d\nu/dt$, due to relative line-of-sight acceleration between the transmitter and the receiver. We searched drift rates in the range $\dot{\nu} \in [-2, +2] \text{ Hz s}^{-1}$ and retained detections with $\text{SNR} \geq 10$.

In our FAST multibeam SETI observations, the central beam continuously tracks the target and is treated as the on-source beam b_{on} , while the remaining beams provide simultaneous off-source references. We denote the set of each off-source beams as $\mathcal{B}_{\text{off}} = \{b_{\text{off},i}\}_i$, where i is the beam number of the off-source beam (here $i=8, 10, 12, 14, 16, 18$). For a dynamic spectrum $x_b(\nu, t)$, we run a Doppler-drift search over trial drift rates and record a finite set of detections. We define *hit* as any detection returned by the search, characterized by its representative frequency ν_0 , trial drift rate $\dot{\nu}_0$, and signal-to-noise ratio SNR_h , satisfying

$$\mathcal{H} \equiv \{h = (\nu_0, \dot{\nu}_0, \text{SNR}_h) : \text{SNR}_h \geq \text{SNR}_{\text{th}} \wedge 0 < |\dot{\nu}_0| \leq \dot{\nu}_{\text{max}}\}. \quad (1)$$

The hits appear in b_{on} is defined as \mathcal{H}_{on} , while those appear in $b_{\text{off},i}$ is defined as $\mathcal{H}_{\text{off},i}$. Following the definition in Traas et al. (2021), the *events* are defined as the set of hit presenting in b_{on} over the scan duration τ_{obs} :

$$\mathcal{E} \equiv \{h \in \mathcal{H}_{\text{on}} : |\nu - \nu_0| \leq |\dot{\nu}_0| \tau_{\text{obs}}\}. \quad (2)$$

Candidate is then defined no hits in \mathcal{B}_{off} :

$$\mathcal{C} \equiv \{\varepsilon(\nu_0, \dot{\nu}_0) \in \mathcal{E} : \forall i, \nexists h' \in \mathcal{H}_{\text{off},i} \text{ s.t. } |\nu - \nu_0| \leq |\dot{\nu}_0| \tau_{\text{obs}}\}. \quad (3)$$

3.1. Hit Matching, Event Grouping and Potential Candidate Selection

In Traas et al. (2021), on-source and off-source scans are acquired sequentially, so the association between detections is established across scans, and an *event* represents a set of hits in the on-source scan that are consistent in frequency-drift space, and *candidate* is defined as event with no hit in all off-source scans. While in our multibeam tracking observations, all beams are recorded simultaneously, removing any temporal offset between on and off measurements. In practice, off-source beams may contain no hits within the Doppler-consistent frequency window of an on-source hit, or contain hits that are not consistent in $(\nu_0, \dot{\nu}_0)$ at the search resolution. Strict constraint for candidate that event with no hit in all off-source scans may cause mismatch of hits.

To avoid this, for each on-source hit $h = (\nu_0, \dot{\nu}_0, \text{SNR}_h) \in \mathcal{H}_{b_{\text{on}}}$, we construct a multibeam event by extracting Doppler-consistent dynamic spectrum segments from the on-source beam and from all simultaneously recorded off-source beams, and grouping them into event by rewritten Eq. (2) as

$$\mathcal{E}_{\text{MB}} \equiv \left\{ \varepsilon_{\text{MB}}(h, x_b) = \left(\begin{array}{c} h(\nu_0, \dot{\nu}_0) \\ \{x_b(\nu, t)\}_{b \in \mathcal{B}_{\text{off}}} \end{array} \right) : h \in \mathcal{H}_{\text{on}} \wedge |\nu - \nu_0| \leq |\dot{\nu}_0| \tau_{\text{obs}} \right\}. \quad (4)$$

For a given on-source hit $h = (\nu_0, \dot{\nu}_0) \in \mathcal{H}_{\text{on}}$ and the i th off-source beam with hit set $\mathcal{H}_{\text{off},i}$, we define a *matched detection* if there exists $h' = (\nu'_0, \dot{\nu}'_0) \in \mathcal{H}_{\text{off},i}$ such that

$$\mathcal{D}_i(\nu_0, \dot{\nu}_0) \equiv \{x_b(\nu, t) : \forall b \in \mathcal{B}_{\text{off}}, \exists h'(\nu'_0, \dot{\nu}'_0) \in \mathcal{H}_{\text{off},i} \text{ s.t. } |\nu'_0 - \nu_0| \leq \delta\nu \wedge |\dot{\nu}'_0 - \dot{\nu}_0| \leq \delta\dot{\nu}\}. \quad (5)$$

where $\delta\dot{\nu} = \delta\nu/\tau_{\text{obs}}$ is the drift rate resolution. And the potential candidate is therefore defined by

$$\mathcal{C}_{\text{MB}} \equiv \{\varepsilon_{\text{MB}}(h, x_b) \in \mathcal{E}_{\text{MB}} : \forall b \in \mathcal{B}_{\text{off}}, x_b \notin \mathcal{D}_i(\nu_0, \dot{\nu}_0)\}. \quad (6)$$

² <https://github.com/UCBerkeleySETI/bliss>

3.2. Hits Filtering

The hits we get after hit searching are not the final hits used for event grouping. Because RFI phenomenology is strongly frequency dependent, we perform clustering independently within coarse frequency intervals. We partition the band into non-overlapping bins of width 50 MHz. Within each bin, we combine on-source hits and the available off beams. To prevent the clustering structure from being dominated by the typically much larger off sample, we downsample the off-source hits to a size comparable to the on-source sample. We then apply Hierarchical Density-Based Spatial Clustering of Applications with Noise (Campello et al. 2013, HDBSCAN) to the standardized feature vectors $(\nu, \dot{\nu}, \log_{10} \text{SNR})$ within each bin. Besides recording the cluster label for each hit, we also record the membership probability that quantifies how strongly a point belongs to its assigned cluster. For each cluster, we additionally compute summary diagnostics such as the cluster size and the on/off composition, including the off fraction

$$f_{\text{off}}(c) = \frac{N_{\text{off}}(c)}{N_{\text{on}}(c) + N_{\text{off}}(c)}, \quad (7)$$

where $N_{\text{on}}(c)$ and $N_{\text{off}}(c)$ denote the numbers of on-source and off-source hits assigned to cluster c , respectively. The on-source hits that fall into clusters with large f_{off} are interpreted as morphologically consistent with the off-source population and thus more likely to be RFI-like, whereas on-source hits assigned to clusters with small f_{off} or labeled as noise are treated as atypical and prioritized for further vetting (here we set the f_{off} threshold of 0.1%).

We also filter the hits by drift rate before potential candidate selection. The drift rates caused by the relative motion of comet in the observation dates are listed in Table 2. Although the MDR we used is 2 Hz s^{-1} in the hit searching, the relative accelerations of the comet are at about $\sim 10^{-5} \text{ Hz s}^{-1}$ level during our observation, and correspond to drift rate of approximately $0.1\text{-}0.2 \text{ Hz s}^{-1}$. The rotation period of 3I/ATLAS is 16.16 hours (Santana-Ros et al. 2025), and the nucleus radius is estimated as $\sim 3 \text{ km}$ (Kareta et al. 2025; Santana-Ros et al. 2025), resulting in a rotational acceleration of $\sim 3.50 \times 10^{-5} \text{ m s}^{-2}$ and corresponding drift rate of $\sim 1.46 \times 10^{-4} \text{ Hz s}^{-1}$, which is two magnitudes of order then the relative accelerations in Table 2, and therefore can be neglected.

Table 2. Accelerations and drift rates of 3I/ATLAS during our observation dates.

Observation Date	$\langle \ddot{\nu} \rangle (\text{km/s}^2)$	$\langle \dot{\nu} \rangle$ at 1250 MHz [Hz s^{-1}]	Used $\langle \dot{\nu} \rangle$ range [Hz s^{-1}]
2025-10-03	2.632×10^{-5}	0.109	(0,0.15)
2025-10-29	2.553×10^{-5}	0.105	(0,0.15)
2025-12-19	4.794×10^{-5}	0.199	(0,0.25)
2026-01-05	5.002×10^{-5}	0.207	(0,0.25)

NOTE—The second and third columns are the mean acceleration and drift rate at central frequency for each observation, the fourth column is the drift rate we used for filtering.

3.3. Significance of SNR

The modified definitions for event also enable us to quantify the significance in SNR between on-source and off-source hits. In multibeam tracking observations, signals appear in multiple beams within a certain frequency range are most probably RFIs. Therefore, beyond the binary criterion of the existence of counterpart off-source hits, we can define a quantitative metric that measures how consistent the strength of the on-source and off-source detections. In particular, a candidate-like signal is expected to be significantly stronger in the on-source beam than in off-source beam, whereas an RFI-like signal tends to show comparable strengths across beams.

During the event grouping, we also record the SNR of the hits in the event. For each off-source dynamic spectrum in the set $\{x_b(\nu, t)\}_{b \in \mathcal{B}_{\text{off}}}$, if there are more than one hits satisfy Eq. (5), we select the hit with the SNR closest to the SNR of corresponding on-source hit among these off-source hits, and its detection status is marked as “1” (All on-source hits are mark as “1”). While if the off-source dynamic spectrum satisfy $x_b \notin \mathcal{D}_i(\nu_0, \dot{\nu}_0)$ within the frequency range, its detection status is marked as “0” and we select the SNR threshold as an upper limit. So potential candidate should be those events with detection status of 1000000. Since there are gain differences between the central beam

and the reference beams, all recorded off-source SNR (and thresholds) are corrected by the gain beam gain ratio $R_b(\nu) \equiv G_b(\nu)/G_{\text{on}}(\nu)$, which can be obtained from the weekly updated antenna gain measurement of FAST³.

Based on statistical analysis of past multibeam observations with SNR threshold of 10 (Tao et al. 2022, 2023; Luan et al. 2025), we can determine that the distribution of SNRs can be modeled by a log-normal distribution $\ln y \sim \mathcal{N}(\mu, \sigma^2)$. We then compare two competing hypotheses for each event: (i) H_R (RFI-like): the SNR values of on-source and off-source are drawn from the same parent distribution; (ii) H_C (candidate-like): the on-source SNR value is systematically stronger than the off-source ensemble by an offset $\Delta \geq 0$. These two hypotheses can be formulated by

$$H_R : \quad \ln y_{\text{on}} \sim \mathcal{N}(\mu, \sigma^2), \quad \ln y_b \sim \mathcal{N}(\mu, \sigma^2), \quad (8)$$

and

$$H_C : \quad \ln y_{\text{on}} \sim \mathcal{N}(\mu + \Delta, \sigma^2), \quad \ln y_b \sim \mathcal{N}(\mu, \sigma^2), \quad \Delta \geq 0. \quad (9)$$

The likelihood for H_R can be written by

$$\mathcal{L}(D | \mu, \sigma, H_R) = p(y_{\text{on}} | \mu, \sigma) \prod_{b \in \mathcal{B}_{\text{det}}} p(y_b | \mu, \sigma) \prod_{b \in \mathcal{B}_{\text{nodet}}} P(y_b \leq L_b | \mu, \sigma), \quad (10)$$

and the likelihood for H_C can be written by

$$\mathcal{L}(D | \mu, \sigma, \Delta, H_C) = p(y_{\text{on}} | \mu + \Delta, \sigma) \prod_{b \in \mathcal{B}_{\text{det}}} p(y_b | \mu, \sigma) \prod_{b \in \mathcal{B}_{\text{nodet}}} P(y_b \leq L_b | \mu, \sigma), \quad (11)$$

where \mathcal{B}_{det} are the beams with detection status of “1”, while $\mathcal{B}_{\text{nodet}}$ are the beams with detection status of “0”. We quantify the strength-contrast evidence via the Bayes factor

$$\text{BF} \equiv \frac{p(D | H_C)}{p(D | H_R)}, \quad (12)$$

where the marginal likelihood under each hypothesis is obtained by integrating over the nuisance parameters,

$$p(D | H_R) = \int p(D | \mu, \sigma, H_R) p(\mu, \sigma) d\mu d\sigma, \quad (13)$$

and

$$p(D | H_C) = \int p(D | \mu, \sigma, \Delta, H_C) p(\mu, \sigma, \Delta) d\mu d\sigma d\Delta. \quad (14)$$

For the hyperparameters μ , σ and Δ , we adopt weakly informative hyperpriors

$$\mu \sim \mathcal{N}(\mu_\mu, s_\mu^2), \quad \sigma \sim \text{HalfNormal}(s_\sigma), \quad \Delta \sim \text{HalfNormal}(s_D), \quad (15)$$

with $(\mu_\mu, s_\mu, s_\sigma)$ estimated from the off-source beams hits in the same observation.

3.4. Structure Tensor

The waterfall plot of a dynamic spectrum may be viewed as a 2-dimension scalar field image $I(\nu, t)$, where each pixel corresponds to (ν_i, t_i) . In the presence of noise, a narrowband signal with a nonzero drift rate introduces locally oriented, anisotropic structure in the (ν, t) plane. Such local orientation can be quantified by the gradient structure tensor (Knutsson et al. 2011), i.e., the second-moment matrix of the image gradients,

$$J(p) \equiv \langle \nabla I(p) \nabla I(p)^T \rangle = \begin{pmatrix} J_{tt} & J_{t\nu} \\ J_{t\nu} & J_{\nu\nu} \end{pmatrix} = \begin{pmatrix} \langle I_t^2 \rangle & \langle I_t I_\nu \rangle \\ \langle I_t I_\nu \rangle & \langle I_\nu^2 \rangle \end{pmatrix}, \quad (16)$$

where $\nabla I = (I_t, I_\nu)^T$ with $I_t \equiv \partial I / \partial t$ and $I_\nu \equiv \partial I / \partial \nu$, and $\langle \cdot \rangle$ denotes a local neighborhood average. The eigenvalues of J are

$$\lambda_{1,2} = \frac{1}{2} \left[(J_{tt} + J_{\nu\nu}) \pm \sqrt{(J_{tt} - J_{\nu\nu})^2 + 4J_{t\nu}^2} \right]. \quad (17)$$

³ <https://fast.bao.ac.cn/cms/category/1977569564215562242>

A convenient scalar measure of local anisotropy is the coherence,

$$C = \frac{\lambda_1 - \lambda_2}{\lambda_1 + \lambda_2}, \quad (18)$$

which ranges from 0 (nearly isotropic texture) to 1 (strongly oriented, line-like structure).

The gradient orientation angle can be written as

$$\theta_g = \frac{1}{2} \arctan \frac{2J_{t\nu}}{J_{tt} - J_{\nu\nu}}, \quad (19)$$

and the orientation of the underlying line-like feature (i.e., the local ridge direction) is orthogonal to the gradient, such that

$$\theta_{\text{line}} = \theta_g + \frac{\pi}{2}. \quad (20)$$

With θ_{line} defined relative to the frequency axis in the (ν, t) plane, the corresponding local slope yields an estimate of the drift rate,

$$\dot{\nu} = \frac{d\nu}{dt} = \tan \theta_{\text{line}} \frac{\delta\nu}{\delta t}, \quad (21)$$

where $\delta\nu/\delta t$ converts pixel units to physical units.

In practice, to improve robustness against noise, we apply two stages of Gaussian smoothing. We first smooth the dynamic spectrum with widths $(\sigma_{\text{pre},t}, \sigma_{\text{pre},\nu})$ before computing numerical gradients, and then compute the tensor components from locally averaged outer products of the gradients using a second smoothing with widths $(\sigma_{\text{st},t}, \sigma_{\text{st},\nu})$. Optionally, a non-negative weight map $w(p)$ may be introduced in the outer products (e.g., based on local signal energy) to emphasize high-power regions when estimating J . Figure 3 illustrates a structure-tensor search and characterization of a simulated drifting narrowband signal by `setigen` (Brzycki et al. 2022) embedded in χ^2 -like noise with a signal line injected to drift at $+0.8 \text{ Hz s}^{-1}$. The signal has a sinc² spectral profile with width $3\delta\nu$, amplitude set to $\text{SNR} = 20$.

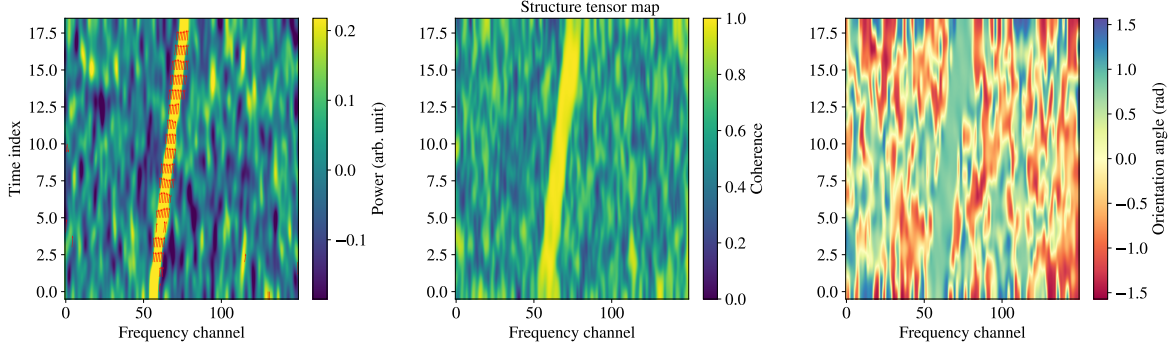


Figure 3. Waterfall plots for a dynamic spectrum with a frequency drifting signal (left), its corresponding coherence map (middle) and orientation angle (right).

Quivers are plotted in the high-coherence region ($\text{coh} > 0.9$), and the contiguous, dense quiver field traces the signal track, and the arrow orientation encodes the sign of the drift rate. The drift rate is estimated from the local orientation angle θ via $\dot{\nu} = (\Delta\nu/\Delta t) \tan \theta \sim 0.75 \text{ Hz s}^{-1}$. Because of finite-difference smoothing and dechirping efficiency < 1 in the algorithm, the recovered $\dot{\nu}$ is expected to be slightly lower than the injected 0.8 Hz s^{-1} .

3.5. Principal Component Analysis

The dynamic spectrum can be also regarded as a 2-dimension matrix $X \in \mathbb{R}^{N_t \times N_\nu}$, then we can extract the principal components (PCs) for this dynamic spectrum, and featurize the drifting signals. PCA is an unsupervised machine-learning method for data decomposition or compression. For our 2-dimension dynamic spectrum matrix, we can use singular value decomposition (SVD) to decompose the matrix into

$$X_c = U \Sigma V^T, \quad (22)$$

where X_c is the matrix after mean bandpass filtering,

$$\mu_j = \frac{1}{N_t} \sum_{i=1}^{N_t} X_{ij}, \quad X_c = X - \mathbf{1}\mu^T, \quad (23)$$

$U \in \mathbb{R}^{N_t \times r}$ and $V \in \mathbb{R}^{N_\nu \times r}$ are the unitary matrix, $\Sigma = \text{diag}(\sigma_1, \dots, \sigma_r)$ is the rectangular diagonal matrix and $r \leq \min(N_t, N_\nu)$ is ranks. Such mean bandpass filtering can efficiently remove the time-invariant (non-drifting) components at each frequency channel. Consequently, stationary carriers and persistent bandpass-like features are strongly suppressed, while frequency-drifting tracks remain in X_c . We can then reconstruct the dynamic spectrum by

$$\widehat{X}_k = U_k \Sigma_k V_k^T + \mathbf{1}\mu^T, \quad (24)$$

with explained-variance ratio $\text{EVR}_k = \sigma_k^2 / \sum_j \sigma_j^2$. The k -th PCs are given by the columns of V ($v_k \in \mathbb{R}^{N_\nu}$), and the corresponding temporal score $S = \Sigma V^T$. For a Doppler-drifting narrowband line in a dynamic spectrum, the EVR of the PCA can be approximated by

$$\text{EVR}_k \propto \exp \left[- \left(\frac{2\pi m w_\nu}{|\dot{\nu}| \tau_{\text{obs}}} \right)^2 \right], \quad m = 0, 1, \dots, \quad (25)$$

where $w_\nu \ll |\dot{\nu}| \tau_{\text{obs}}$ denotes the effective linewidth in frequency of the drifting feature. We further define the EVR entropy as

$$H_{\text{EVR}} = - \sum_k p_k \ln p_k, \quad p_k = \frac{\text{EVR}_k}{\sum_j \text{EVR}_j}. \quad (26)$$

Under the above approximation, the EVR entropy of a drifting line can be expressed as

$$H_{\text{EVR}} \approx \ln \left(\frac{|\dot{\nu}| \tau_{\text{obs}}}{2\pi w_\nu} \right) + \frac{1}{2} \ln(\pi e). \quad (27)$$

The detailed derivations of the PCA for Doppler-drifting signal are in Appendix A. Figure 4 is the PCA summary for a simulated drifting signal used in Section 3.4. For a drifting narrowband signal, a certain number of PCs typically captures a coherent spectral pattern $v_k(\nu)$ and a smoothly varying temporal score $S_k(t)$, producing a compact representation in EVR. The EVR entropy for the simulated signal is 2.655, which is modestly larger than the theoretical approximation values 2.243 in Eq. (27) with $w_\nu \approx \delta\nu$. Because the data do not perfectly follow the idealized, shift-invariant Gaussian-kernel model, the EVR distribution becomes slightly less concentrated than the analytic limit. Finite drift span and edge truncation can introduce discrete spectral leakage, small time variability in the line amplitude or profile can spread power across additional modes, and residual correlated noise or spectral texture can further transfer variance into higher-order PCs. Together, these effects raise the measured H_{EVR} modestly above the theoretical estimate.

3.6. Overall Workflow

The overall data analysis processes are illustrated in Figure 5. Before the finding hits step with `bliss_find_hits`, the raw sdfits data are converted into HDF5 format by `blimpy` (Price et al. 2019). The `fits` files are archived for each beam, each `fits` file corresponds to a different sample time segment of the observation. For each beam, these `fits` files are time-ordered, concatenated along the time axis, and then converted into an HDF5 product containing two-dimensional time-frequency power spectra for four polarization channels, XX, YY, XY and YX, which are derived from self-correlation and cross correlation of the data in two orthogonal linear polarization directions X and Y.

In this work, we perform an independent narrowband Doppler-drift search on each of the four polarization channels, following the procedure outlined in Figure 5. For each channel, we generate a list of potential candidates and inspect them using standard dynamic spectrum (waterfall plot) visualizations to assess whether they meet the criteria in Eq. (6). This assessment is complemented by structure-tensor diagnostics and PCA summary plots, which provide additional feature-based characterization of the signals. We then quantify the physical and statistical properties of the resulting sample using dedicated statistical analyses.

On scan patch PCA summary

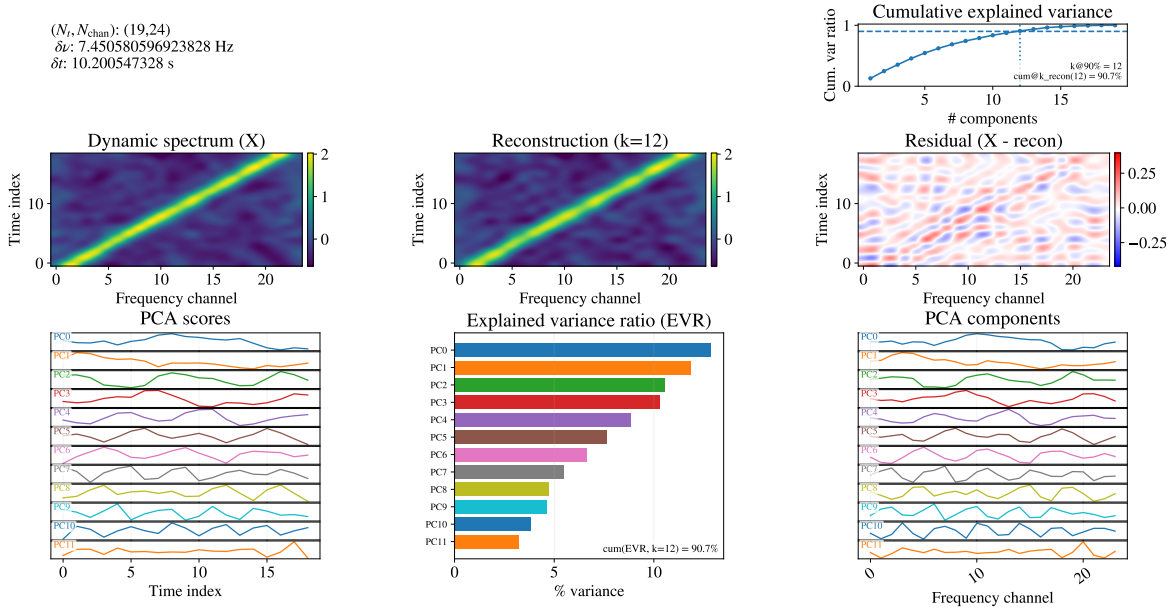


Figure 4. PCA summary for the drifting signal. Top row: metadata for this panel (left) and the cumulative explained variance ratio (right). The vertical dotted line marks the minimum number of PCs required to reach $\text{CEV} \geq 0.90$. Middle row: the original dynamic spectrum (left), its rank- k_{recon} reconstruction $\hat{X}_{k_{\text{recon}}}$ (center), and the residual $X - \hat{X}_{k_{\text{recon}}}$ (right). Bottom row: PCA diagnostics for the first k_{recon} temporal scores $S_k(t)$ (left), explained variance ratio EVR_k (center), and spectral components $v_k(\nu)$ (right). Scores and components are normalized for display, the color scheme is consistent across the three bottom panels for each PC.

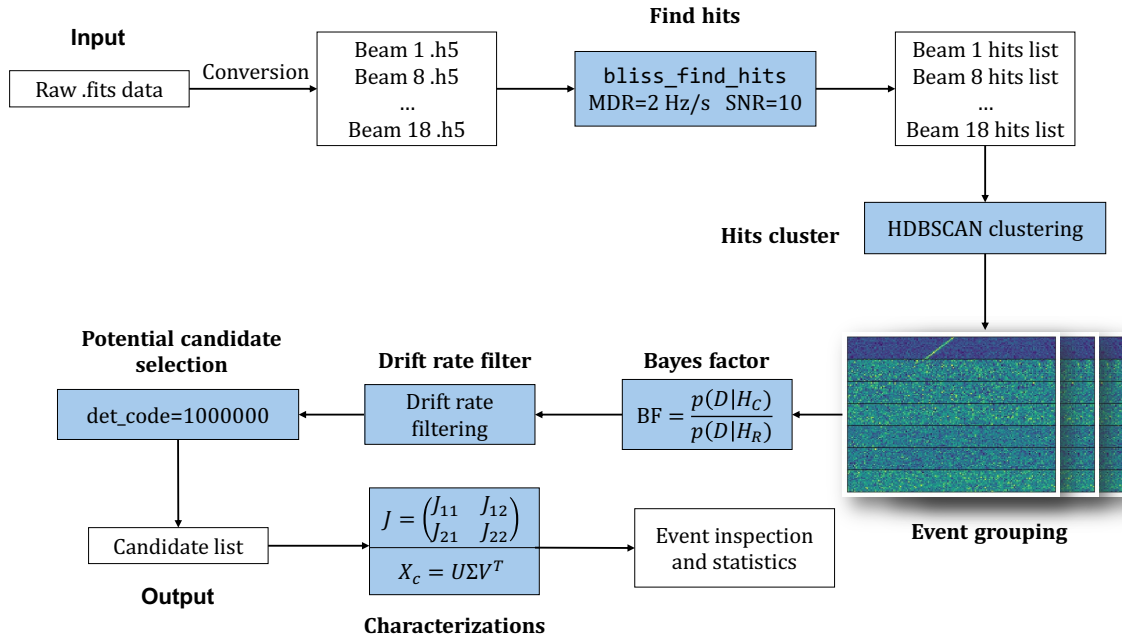


Figure 5. A schematic representation of our workflow for the data analysis.

4. RESULTS

The general number statistics for hits, events and potential candidates in this narrowband drifting signal search are listed in Table 3. About 40% hits fall in the frequency ranges of civil aviation and navigation satellites, implying that a considerable amount of RFIs may come from these known sources.

Table 3. Numbers of hits, events and potential candidate in the narrowband drifting signal search.

Polarization	Hits number	Event number	Hits in civil and GNSS (%)	Candidate number
XX	7524031	1079020	2.23, 35.97	1662
YY	7355950	1061361	2.46, 33.57	2028
XY	2832144	124943	2.22, 37.66	7216
YX	2316772	443614	1.91, 36.13	3386

NOTE—The fourth column is the percentages of hits falling in the frequency range of civil aviation and global navigation satellite system (GNSS), respectively.

The distributions of hits and events in frequency, drift rate, and signal-to-noise ratio for each polarization channel are illustrated in Figure 6, and some known RFI sources within the observation frequency ranges (Wang et al. 2021) are also shown in the plots. The slight negative drift rate bias is caused by the downward relative acceleration of non-geosynchronous satellites Zhang et al. (2006).

We further investigate the distribution of potential candidates by the scatter plot in Figure 7. A large fraction of potential candidates cluster within several restricted frequency windows rather than being uniformly distributed across the band. In particular, prominent concentrations coincide with the civil aviation band and the navigation satellites. The drift rates span a broad range, forming an overall band-like distribution, suggesting that these potential candidates are likely dominated by RFI with similar phenomenology.

All selected potential candidates are reexamined by a visual inspection of the dynamic spectra. Almost all the potential candidates are false positives mentioned in Tao et al. (2022), which can be directly excluded. Specifically, those potential candidates fall at the expected drift rates in Figure 7 are also filtered during the visual inspection. Five potential candidates survive after visual inspection, and exhibit similar “chirp-up” feature, instead of constant linear drift, which are listed in Table 4. All these five chirp-up signal are found in the observation on 5 January 2026.

Table 4. Frequencies and drift rates of the five chirp-up potential candidates.

Event ID	Central Frequency [MHz]	Drift rate [Hz s^{-1}]	Polarization channel
250	1431.9978	0.045	XX
3703	1250.0126	0.055	YX
5965	1333.3168	0.135	YY
47992	1250.0126	0.047	YY
225671	1066.6534	0.115	YY

Figure 8 (a) illustrates an example of these chirp-up drifting signals (Other four chirp-up potential candidates are shown in Appendix B). We also identify a potential candidate exhibiting a chirp-up morphology, however, a morphologically similar signal is present in the reference beam (See Figure 8 (b)). We therefore reject this as RFI, which suggests that the chirp-up signals may share a common instrumental origin. Motivated by this, we investigate whether the observed chirp-up frequencies can be explained as intermodulation products of the nominal clock-oscillator frequencies used on

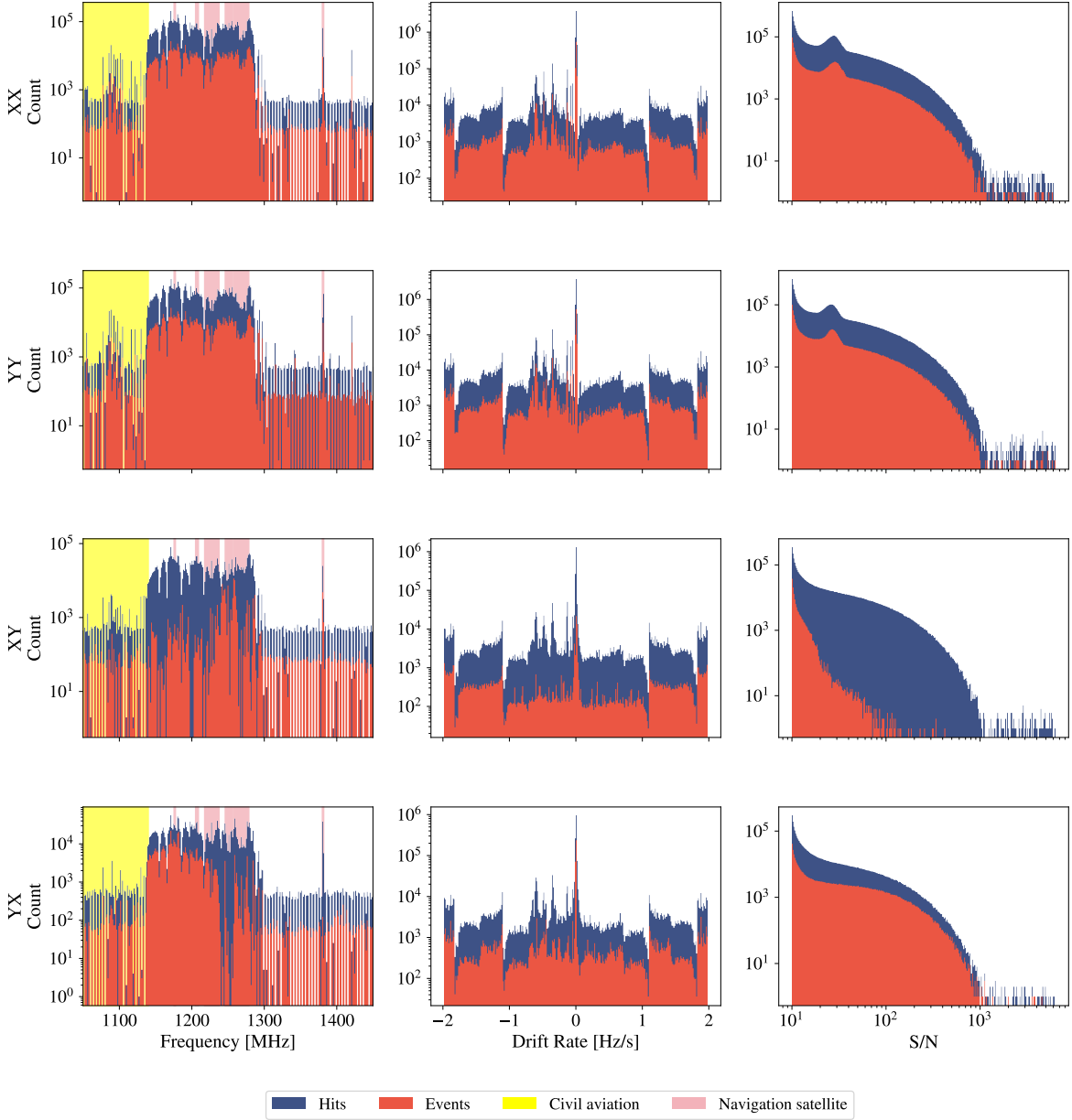


Figure 6. Histograms of the distributions of frequency (left column), drift rate (middle column) and signal-to-noise ratio (right column) for the four polarization channels.

the ROACH 2 FPGA board.⁴ Specifically, we consider integer linear combinations of the form $\nu = m\nu_1 + n\nu_2$, where ν_1 and ν_2 are candidate oscillator frequencies and m and n are non-negative integers. By scanning over (ν_1, ν_2, m, n) , we construct intermodulation sequences and assess whether they can account for the measured frequencies of the chirp-up signal. Figure 9 summarizes the best-matching pairings for these signals. All five frequencies admits one or more such explanations within absolute residual $|\nu_{\text{model}} - \nu_{\text{obs}}| \leq 0.03\text{MHz}$. Moreover, the solution sets overlap across different frequencies in terms of the oscillator frequency pairs, indicating that the five signals can be linked through a common clock oscillator frequency library. This behavior is consistent with an instrumental (clock-related intermodulation) RFI origin. Additionally, since there is currently no evidence indicating any abnormal acceleration variations in the

⁴ The nominal frequencies of all crystal oscillators used on ROACH2 are listed at https://github.com/ska-sa/roach2_hardware/blob/master/release/rev2/A/BOM/ROACH-2_REV2_BOM.csv.

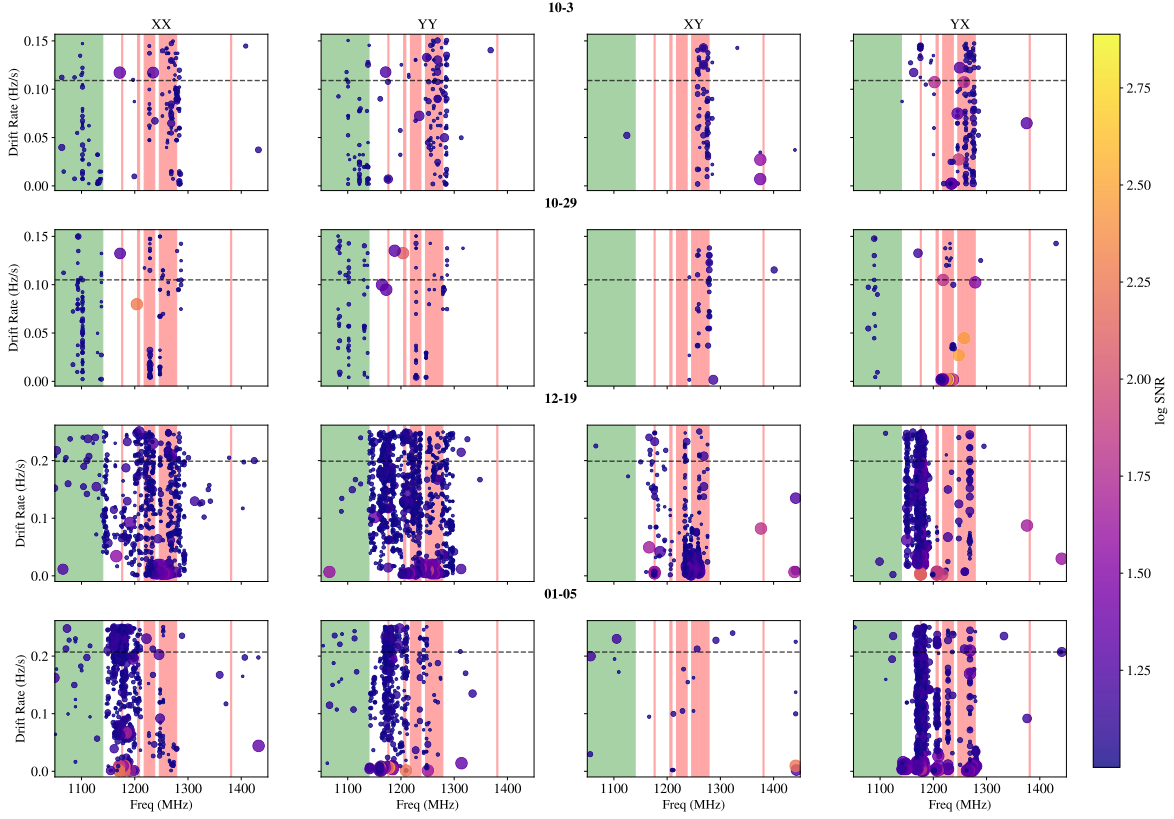


Figure 7. Scatter plots of potential candidate in frequency, drift rate and signal-to-noise ratio for each polarization channel. The color and the size for each point represent the value of SNR in log space. The green and red color bar is the frequency ranges of civil aviation and navigation satellites, respectively. The black dashed lines represent the expected drift rates for each observation date.

3I/ATLAS, and the drift rates of these signals do not align with the expected drift rate for 5 January 2026, finally, we are inclined to classify these signals as RFI.

5. DISCUSSION

5.1. Sensitivity

The sensitivity of a radio observation can be determined by system equivalent flux density (Wilson et al. 2013; Thompson et al. 2017)

$$\text{SEFD} = \frac{2k_{\text{B}}T_{\text{sys}}}{A_{\text{eff}}}, \quad (28)$$

where k_{B} is the Boltzmann constant, T_{sys} is the system temperature, and A_{eff} is the effective collecting area. The sensitivity $A_{\text{eff}}/T_{\text{sys}}$ of FAST L-band 19 beam receiver is $\sim 2000 \text{ m}^2 \text{ K}^{-1}$ (Nan et al. 2011; Li & Pan 2016; Jiang et al. 2019). For narrowband signal detection (i.e., the signal bandwidth is narrower or equal to the observing spectral resolution), the minimum detectable flux density S_{min} can be given by (Enriquez et al. 2017)

$$S_{\text{min}} = \text{SNR}_{\text{min}} \frac{\text{SEFD}}{\beta} \sqrt{\frac{\delta\nu_{\text{ch}}}{n_{\text{pol}}\tau_{\text{obs}}}}, \quad (29)$$

where SNR_{min} is the signal-to-noise ratio threshold, τ_{obs} is the effective observing duration, $\delta\nu_{\text{ch}}$ is the frequency channel bandwidth, n_{pol} represents the number of polarization channels of the telescope and β is the dechirping efficiency expressed as

$$\beta = \begin{cases} 1 & |\dot{\nu}| \leq 0 \\ \frac{\delta\nu}{|\dot{\nu}|\delta t} & |\dot{\nu}| > \frac{\delta\nu}{\delta t} \end{cases}. \quad (30)$$

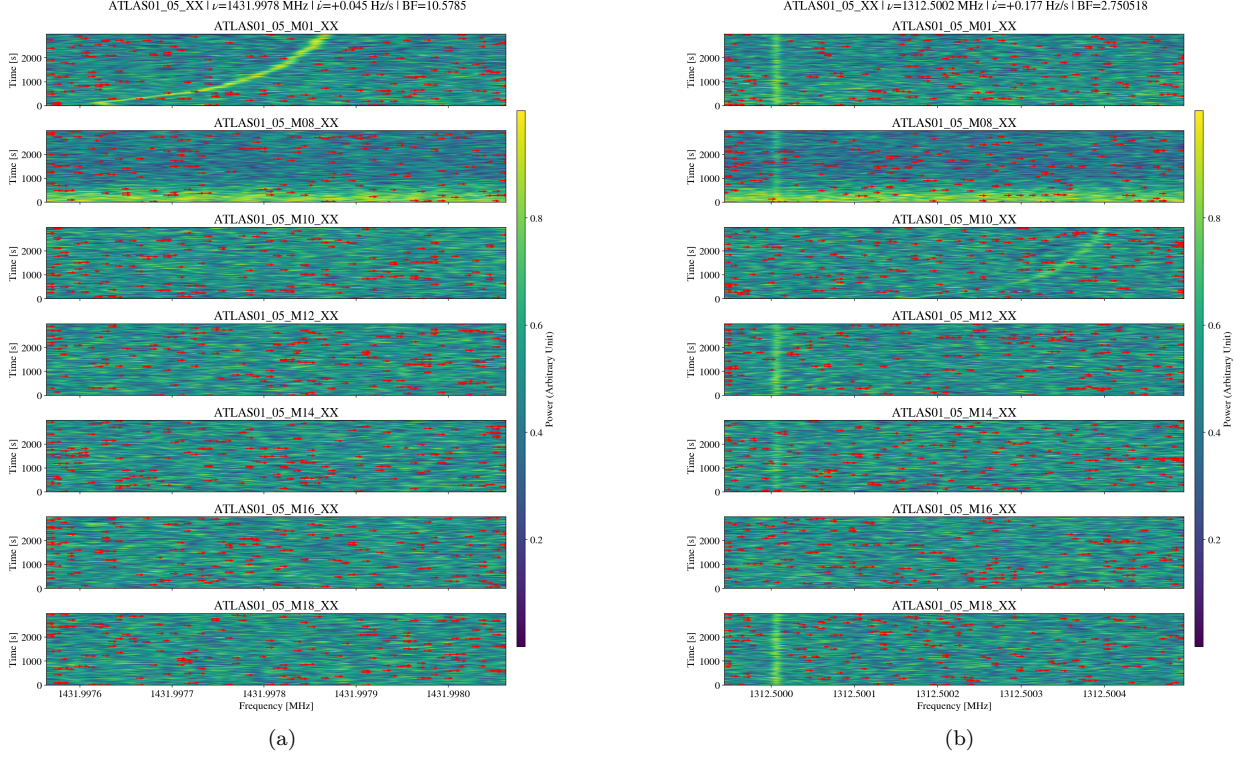


Figure 8. (a) A chirp-up signal at frequency 1431.9978 MHz, with a drift rate of 0.045 Hz s^{-1} given by `bliss`. The chirp-up signal only appears in the central beam, while no obvious corresponding drifting signals appear in any reference beam. (b) A chirp-up signal at 1312.5002 MHz absent in the central beam, but appears in one of the reference beams.

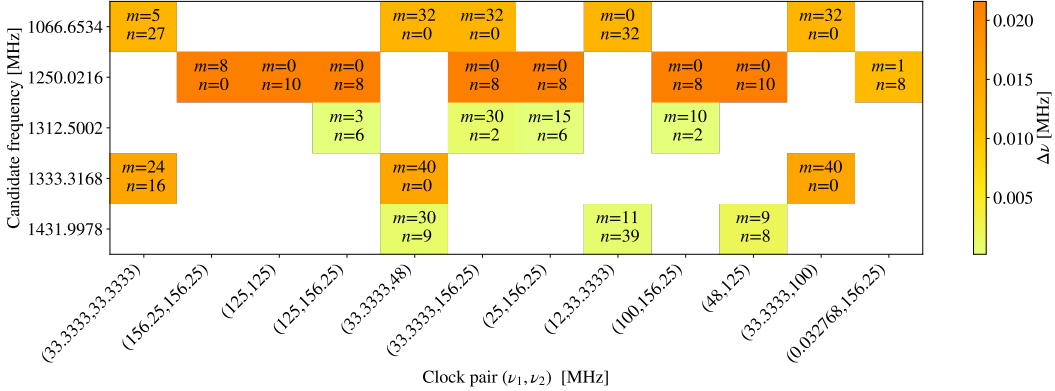


Figure 9. Intermodulation analysis for the chirp-up signal frequencies. The horizontal axis lists the clock-frequency pairs (ν_i, ν_j) , and each row corresponds to one signal frequency ν_{obs} . Each cell reports the integers (m, n) of the best match $\nu_{\text{model}} = m\nu_1 + n\nu_2$ (with $m, n \geq 0$ and $m + n \leq 50$). The colormap shows the absolute residual $|\nu_{\text{model}} - \nu_{\text{obs}}|$.

The minimum detectable flux density can be used to estimate the minimum luminosity detection threshold based on the distance of the source d , which can be quantified by equivalent isotropic radiated power (EIRP) of the antenna:

$$\text{EIRP} = 4\pi d^2 S_{\text{min}} \delta\nu_t, \quad (31)$$

where $\delta\nu_t$ is the transmitted signal width (We assume to be $\delta\nu_t \sim 1 \text{ Hz}$). Based on the distances and our observation configurations, the EIRP is estimated to be $\sim 10^{-3} \text{ W}$ for our observations. We also define an Earth-directed EIRP

per steradian $L_\Omega \equiv \text{EIRP}/\Omega_\oplus$ as a comparative indicator for a hypothetical Earth-pointing transmitter, where

$$\Omega_\oplus(d) = 2\pi(1 - \cos \alpha), \quad \sin \alpha = \frac{R_\oplus}{d} \quad (32)$$

is the solid angle corresponding to the Earth as seen from 3I/ATLAS, with R_\oplus being the radius of Earth. The EIRP values and the Earth-directed EIRP values per steradian are listed in Table 5.

Table 5. EIRP values, solid angle of Earth, and the Earth-directed EIRP per steradian of 3I/ATLAS during our observation dates.

Observation Date	EIRP (W)	Ω_\oplus	L_Ω
2025-10-03	5.497×10^{-3}	1.025×10^{-3}	5.364
2025-10-29	4.727×10^{-3}	1.192×10^{-3}	3.966
2025-12-19	2.862×10^{-3}	1.968×10^{-3}	1.454
2026-01-05	3.349×10^{-3}	1.682×10^{-3}	1.991

5.2. Bayesian Limits on the Detection of Technosignatures

We consider the hypothesis that a comet may host a narrowband radio transmitter with a small prior probability p_T . Let $T \in \{0, 1\}$ denote latent indicator of whether the target hosts a narrowband transmitter ($T = 1$) or not ($T = 0$). For a radio transmitter with EIRP strength parameter $L > 0$, the single-trial detection probability to detect the signal from the transmitter can be given by

$$\mathcal{P}_{\text{det}}(L) = \Phi(cL - \text{SNR}_{\text{th}}), \quad (33)$$

where c collects the instrumental sensitivity, integration time, spectral resolution, and target distance dependence, $\Phi(x)$ is the standard normal cumulative distribution function. For the k -th observing configuration, we define the single-trial detection probability given L as $\mathcal{P}_{\text{det},k}(L)$. Under the assumption that trials are independent conditioned on (T, L) , the likelihood of observing all-zero outcomes given $T = 1$ and L is

$$\mathcal{L}(\text{all0} | T = 1, L) = \prod_{k=1}^K [1 - \mathcal{P}_{\text{det},k}(L)]^{N_k}. \quad (34)$$

While for $T = 0$, the likelihood is

$$\mathcal{L}(\text{all0} | T = 0) = 1. \quad (35)$$

The joint posterior $p(p_T, L | \text{all0})$ can be given by

$$p(p_T, L | \text{all0}) = \frac{\mathcal{L}(\text{all0} | T = 1, L)\pi(L)p_T\pi(p_T)}{p(\text{all0})}, \quad (36)$$

where $p(\text{all0})$ is the evidence of all-zero observation result, $\pi(p_T)$ is the prior of p_T and $\pi(L)$ is the prior of L . The details derivations for above equations are given in Appendix C.1. Apart from the all-zero result in this work, we also include the observation configurations of null results in ATA (Sheikh et al. 2025), GBT (Jacobson-Bell et al. 2025) and MeerKAT Pisano et al. (2025) for joint constraints. The SEFD of ATA are fitted by the values for different center frequencies.

5.2.1. Priors for Transmitter Occurrence Probability and EIRP

The analysis above requires specifying priors for the transmitter occurrence probability p_T and the transmitter EIRP L . We adopt simple prior families designed to encode only two minimal expectations. The probability that a given target hosts an active narrowband transmitter is small ($p_T \ll 1$), while its order of magnitude remains uncertain.

Accordingly, we use flexible distributions on p_T that concentrate most prior mass at low values yet do not enforce a single characteristic scale. Specifically, we explore two alternative choices for p_T : (i) a scaled-beta prior, in which $q \sim \text{Beta}(a, b)$ and $p_T = p_{T,\max}q$, thereby enforcing $0 < p_T \leq p_{T,\max}$ while allowing the concentration toward small p_T to be tuned by (a, b) ; and (ii) a logit-normal prior, in which $z \sim \mathcal{N}(\mu_p, \sigma_p^2)$ and $p_T = p_{T,\max} \text{sigmoid}(z)$, equivalently representing a logit-normal prior rescaled to $(0, p_{T,\max})$. The EIRP of the transmitter on the comet is not expected to be extreme, but it may plausibly span a relatively small orders of magnitude, this motivates placing a log-normal prior $\ln L \sim \mathcal{N}(\mu_L, \sigma_L^2)$, so that multiplicative uncertainty is represented naturally. These assumptions are deliberately conservative and are used to illustrate how non-detections map to constraints on (p_T, L) .

We report constraints using marginal posteriors obtained from the joint posterior $p(p_T, L \mid \text{all0})$ by integrating out the other parameter. Concretely, we summarize $p(p_T \mid \text{all0})$ (marginalizing over L) and $p(L \mid \text{all0})$ (marginalizing over p_T) via posterior point estimates and central credible intervals. With the adopted parameter choices (listed in Appendix C.2), both the scaled-beta and the scaled logit-normal priors for p_T yield consistent constraints, $\log_{10} p_T = -2.301^{+0.301}_{-0.196}$ (68% credible interval), while the log-normal prior for L yields $\log_{10} L = 0.000^{+2.000}_{-0.725}$ (68% credible interval). We summarize the marginal posteriors using the posterior median and the 68% highest-posterior-density (HPD) interval. The primary information of all-zero result is from Eq. (34), when $p_T \ll 1$ and/or $\mathcal{P}_{\text{det},k}(L)$ is overall small within the prior-supported range, the posterior remains prior-dominated and different observing configurations yield similar marginal constraints.

5.2.2. Hierarchical Priors Models

To avoid over-committing to a single, fixed prior scale for the transmitter occurrence probability and EIRP in the weak-information (all-zero) regime, we adopt hierarchical prior families in which the distributional shape parameters are themselves treated as unknowns and inferred jointly with the quantities of interest.

We implement two hierarchical variants consistent with the previous non-hierarchical priors: (i) hierarchical scale-beta prior, in which

$$q \mid m, \kappa \sim \text{Beta}(m\kappa, (1-m)\kappa). \quad (37)$$

Here $m \in (0, 1)$ controls the prior mean of q through $\mathbb{E}(q \mid m, \kappa) = m$, while $\kappa > 0$ controls the prior concentration (or dispersion) around m , and larger κ yields a more concentrated prior and smaller κ yields a more diffuse prior. We complete the hierarchical model by assigning hyperpriors

$$m \sim \text{Beta}(\alpha_m, \beta_m), \quad \kappa \sim \text{Gamma}(a_\kappa, b_\kappa), \quad (38)$$

where the Gamma distribution is parameterized by shape a_κ and rate b_κ . (ii) hierarchical logit-normal prior, in which

$$z \mid \mu_p, \sigma_p \sim \mathcal{N}(\mu_p, \sigma_p^2), \quad (39)$$

where $p_T = p_{T,\max} \text{sigmoid}(z)$, and assign hyperpriors to (μ_p, σ_p) ,

$$\mu_p \sim \mathcal{N}(\mu_{p,0}, \tau_{\mu_p}^2), \quad \sigma_p \sim \text{HalfNormal}(s_{\sigma_p}). \quad (40)$$

In this hierarchical model, μ_p controls the typical scale of p_T in logit space, while σ_p controls the dispersion of p_T implied by the prior. The log-normal hyperprior on σ_p ensures positivity and allows the width of the logit-scale distribution to be inferred rather than fixed.

For the transmitter EIRP, we adopt a hierarchical log-normal family to represent multiplicative uncertainty over orders of magnitude,

$$\ln L \mid \mu_L, \sigma_L \sim \mathcal{N}(\mu_L, \sigma_L^2), \quad (41)$$

with hyperpriors on the location and scale parameters,

$$\mu_L \sim \mathcal{N}(\mu_{L,0}, \tau_{\mu_L}^2), \quad \ln \sigma_L \sim \mathcal{N}(\ln \sigma_{L,0}, \tau_{\ln \sigma_L}^2), \quad (42)$$

which represents multiplicative uncertainty in L naturally on a logarithmic scale.

In the all-zero detection regime, the constraints on (p_T, L) are driven primarily by the transitions of detection probability $\mathcal{P}_{\text{det}}(L)$. The different values of L that would be weakly constrained by one configuration can be strongly suppressed by another, and the combined likelihood in Eq. (34), consequently shrinks the allowed region in the

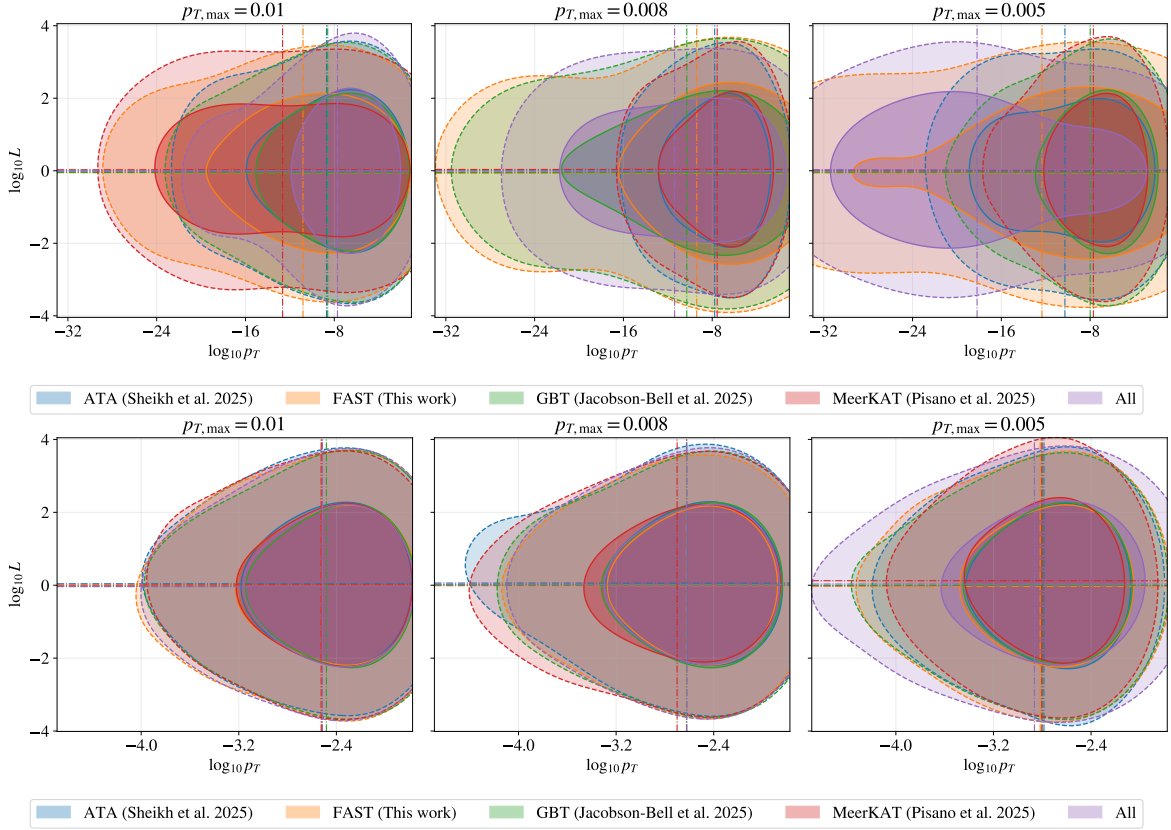


Figure 10. Contours for the scaled-beta (top) and logit-normal (bottom) p_T , with lognormal L in \log_{10} space under the all-zero detection with different $p_{T,\max}$ setting. The contours show the joint posterior densities marginalized over nuisance parameters for the observing configurations in ATA, GBT, MeerKAT and this work. Solid and dashed curves enclose the 68% and 95% HPD regions, respectively.

$\log_{10} p_T - \log_{10} L$ plane, producing a tighter credible region. The scaled-beta prior typically exhibits a larger apparent sensitivity of the $\log_{10} p_T - \log_{10} L$ contours to changes in $p_{T,\max}$, whereas logit-normal mapping tends to redistribute probability more smoothly in $\log p_T$, leading to comparatively smaller morphological changes in the inferred joint credible region (See Figure 10).

Configurations with observations taken on adjacent dates (hence similar comet distances) tend to yield more consistent $\mathcal{P}_{\text{det}}(L)$ across epochs. The resulting likelihood factors constrain essentially the same L -range repeatedly, producing more coherent suppression in the (p_T, L) plane and therefore comparatively tighter $\log_{10} p_T - \log_{10} L$ credible regions. By contrast, configurations spanning widely separated dates probe substantially different distances and sensitivity scalings, which tends to preserve a stronger $\log_{10} p_T - \log_{10} L$ degeneracy and leads to broader, more elongated contours. The effect is particularly apparent under the scaled-beta prior, which can concentrate posterior mass near the imposed upper bound $p_{T,\max}$.

In this work, our observation dates are set on relatively discontinuous days, and the total time span is also quite long, therefore yield transition regions in Eq. (33) that collectively span a broader range of L than configurations of the single-epoch observation of GBT and MeerKAT in one day, and the multiple observations of ATA in relatively continuous days. When the three telescopes are combined, the joint likelihood effectively stacks heterogeneous sensitivity curves in L , which ultimately tightens the allowed (p_T, L) region. At larger $p_{T,\max}$ the scaled-beta prior admits substantial prior volume at higher p_T , and the joint posterior can initially appear broader as probability mass redistributes along the remaining (p_T, L) degeneracy before the compounded likelihood dominates. As $p_{T,\max}$ is decreased, this high- p_T volume is progressively removed and the joint HPD region contracts accordingly. The constraint results for p_T and L for each observation are listed in Table 6.

Table 6. Results of the parameter best fits, marginalized medians and 68 % errors from our models with $p_{T,\max} = 0.005$ for scaled-beta $p_T + \text{lognormal } L$ (first and third columns) and logit-normal $p_T + \text{lognormal } L$ (second and fourth columns).

Observation	$\log_{10} p_T$ (scaled-beta)	$\log_{10} p_T$ (logit-normal)	$\log_{10} L$ (scaled-beta)	$\log_{10} L$ (logit-normal)
ATA (Sheikh et al. 2025)	$-6.742^{+2.700}_{-9.094}$	$-2.566^{+0.297}_{-0.504}$	$0.019^{+1.288}_{-1.281}$	$0.059^{+1.288}_{-1.337}$
FAST (This work)	$-7.892^{+6.411}_{-7.730}$	$-2.558^{+0.311}_{-0.454}$	$-0.026^{+1.254}_{-1.295}$	$-0.066^{+1.322}_{-1.225}$
GBT (Jacobson-Bell et al. 2025)	$-6.240^{+2.739}_{-3.542}$	$-2.571^{+0.304}_{-0.484}$	$-0.033^{+1.260}_{-1.255}$	$-0.001^{+1.261}_{-1.335}$
MeerKAT Pisano et al. (2025)	$-6.128^{+1.997}_{-3.580}$	$-2.610^{+0.343}_{-0.542}$	$0.013^{+1.273}_{-1.278}$	$0.004^{+1.276}_{-1.334}$
All	$-20.456^{+14.083}_{-8.247}$	$-2.574^{+0.319}_{-0.476}$	$0.018^{+1.285}_{-1.295}$	$-0.075^{+1.361}_{-1.262}$

Finally, we emphasize that the purpose of these priors is not to claim a physically unique distribution for either p_T or L , but to provide illustrative parameterizations demonstrating how non-detections map to make constraints on transmitter occurrence probability and the transmitter EIRP.

5.3. Events Featurization

Although most of the events are false positives, we still make statistical analysis for the Bayes Factor, coherence and PCA for them, so that we can investigate the characteristics for these false positives. We first summarize the empirical distributions of the Bayes factor in Figure 11 across polarization products and band categories. The four polarization channels exhibit markedly different BF distributions: XX and YY are predominantly negative with modest tails, whereas the cross-polarization products (XY/YX) are broader and more multimodal, with a substantial fraction extending to $\ln \text{BF} > 0$. A similar dependence is observed across frequency categories: GNSS-rich regions show heavy-tailed, multimodal BF distributions, consistent with heterogeneous interference morphologies, while the civil-aviation band appears comparatively more homogeneous.

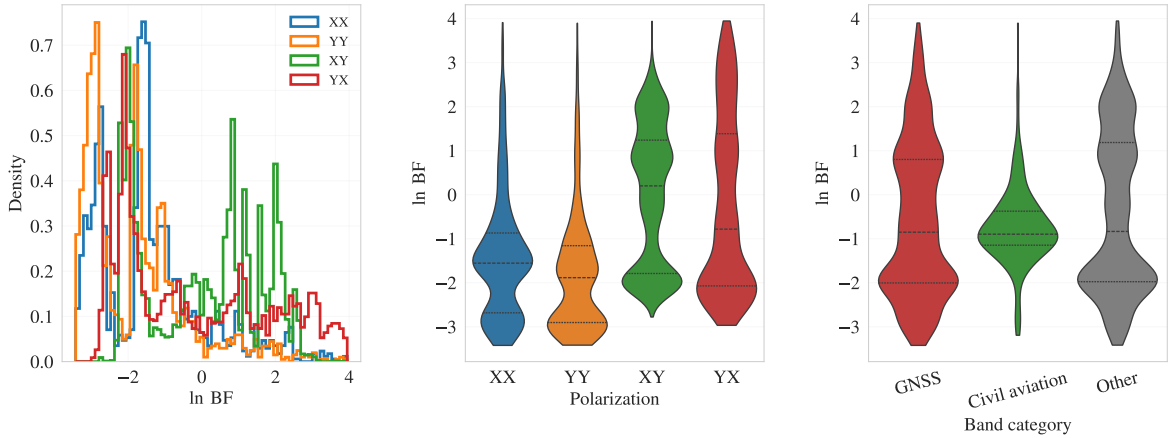


Figure 11. Distribution of the Bayes factor for potential candidates. Left: density histograms of for $\ln \text{BF}$ the four polarization products (XX, YY, XY, YX). Middle: violin plots of $\ln \text{BF}$ grouped by polarization product (dashed lines indicate quartiles). Right: violin plots of $\ln \text{BF}$ grouped by frequency-band category.

The statistics for the outputs resulting from structure tensor and PCA are illustrated in Figure 12. These features of the dynamic spectra in all beams of each event are stratified by polarization channel and by on/off beam. As we described in Section 3.4, we select high-coherence regions to place the structure tensor quiver arrows. This restriction is intended to preferentially select locally anisotropic patches that, in an ideal narrowband drifting signal, would concentrate around the drift track and thereby highlight its linear geometry. If the selected region is dominated by a single, stable linear structure, coh within that region should be relatively uniform and $\text{Var}(\text{coh})$ should be small. Therefore, $\text{Var}(\text{coh})$ can be interpreted as a quality-control indicator for whether the selected high-coherence region behaves like a coherent instead aggregates multiple texture-driven patches. The line-orientation estimator θ_{line}

has group medians close to zero with modest dispersion, whereas $\text{Var}(\theta)$ shows a long-tailed distribution, which is consistent with the characteristics of textured backgrounds or multi-component structures where no single drift-like ridge dominates the patch (See the examples of six event waterfall plots in Figure 8 and Figure 14, almost all quiver arrows are horizontal without any significant inclination).

The EVR entropy H_{EVR} is systematically lower for the cross-hands (XY/YX) than for XX/YY, implying that the EVR distribution is more peaked toward the first few PCs (i.e., a smaller effective rank r_{eff}). This trend is consistent with low-rank structure. The component-to-component ratios $\ln(\text{EVR}_k/\text{EVR}_{k+1})$ decrease rapidly with k and approach a near-flat tail at larger k , showing that the PCA spectrum transitions from a steep leading part to a noise-dominated regime. Finally, the goodness-of-fit R^2 for the quadratic model $\ln(\text{EVR}_m)$ varies substantially by group, with generally higher R^2 in the cross-hands products, indicating that those channels more often follow a smooth, rapidly decaying EVR envelope over the fitted range.

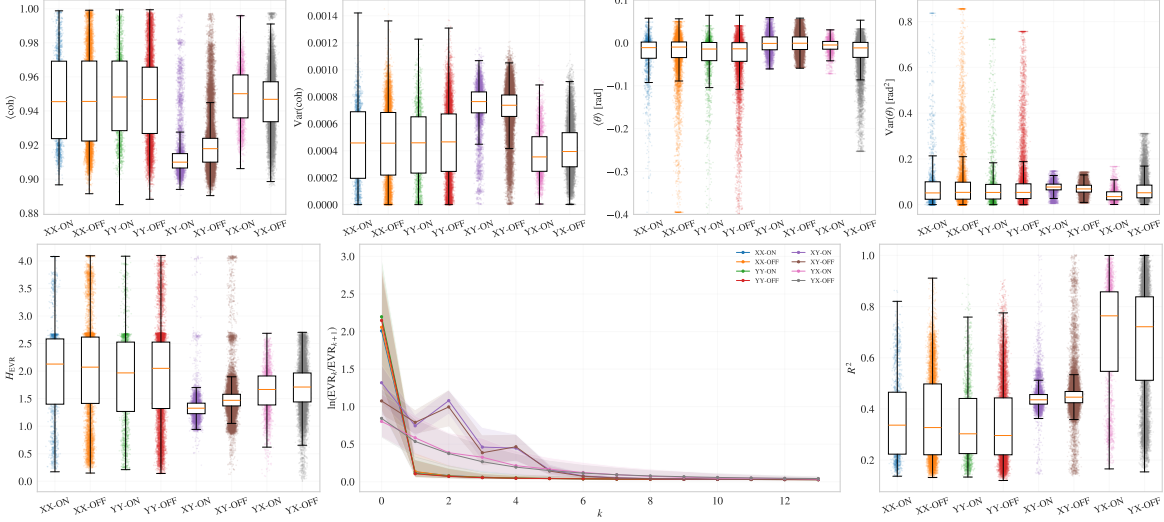


Figure 12. Distributions of feature diagnostics derived from the structure tensor and PCA for the potential candidates in all beams, grouped by polarization channels and beams (ON: central beam; OFF: reference beams). Top row: structure tensor statistics computed on the selected high-coherence regions, $\langle \text{coh} \rangle$ and $\text{Var}(\text{coh})$, as well as line orientation angle, $\langle \theta \rangle$ and $\text{Var}(\theta)$. Bottom row: EVR entropy H_{EVR} , median trend of EVR ratio $\ln(\text{EVR}_k/\text{EVR}_{k+1})$ versus k (curves show per-group medians and shaded regions show the interquartile range) and the coefficient of determination R^2 from fitting $\ln(\text{EVR}_m)$ across available components. Box plots summarize per-group distributions (median, IQR, and $1.5 \times \text{IQR}$ whiskers) and colored points show individual samples in each group.

Because the vast majority of the present sample consists of false positives and complex RFI or background noise, these statistics primarily reflect the background texture and instrumental/RFI imprint within the dynamic spectrum cutouts, rather than isolating the idealized signature of a single, clean Doppler-drifting narrowband track. A notable outcome is that the ON and OFF beams exhibit broadly similar population-level distributions for these features. This consistency is aligned with the fact that the vast majority of detections in the present sample are false positives: the dominant contribution to these statistics is therefore the morphology of background noise texture and persistent instrumental/RFI. At the same time, the nontrivial coherence levels and structured EVR patterns indicate that these RFI/noise realizations are not featureless. They often contain anisotropic and low-rank components that are quantified by the same diagnostics, and which must be accounted for when interpreting drifting-signal features.

We also identify a plausible reason why visually apparent drifting tracks are not consistently traced by the structure-tensor quiver arrows. Coherence measure is derived from locally averaged second moments of the intensity gradients, and thus quantifies local anisotropy. In real dynamic spectrum, many visually apparent signal with drift-like features often show amplitude modulation and intermittency along the track, whereas the background often contains stable instrumental/RFI texture (e.g., quasi-horizontal striations). Under our high-coherence sampling strategy, the selected pixels preferentially trace the most repeatable anisotropic texture within each patch, which frequently aligns close to the frequency axis, yielding $\langle \theta \rangle$ concentrated near zero even when a drift-like pattern signal is present. Figure 13 illustrates this behavior using two representative false-positive events that appear in all beams: one contains a

visually clear linear drift, and the other is a relatively broadband horizontal feature. Although the drift is visible in both the waterfall and the orientation-angle map, its intermittency leads to spatially fragmented coherence, so the sampled quivers do not follow the track continuously. By contrast, the broadband horizontal feature is more uniform and produces a stronger, more spatially coherent anisotropic signature, and is therefore more reliably emphasized by the quiver arrows.

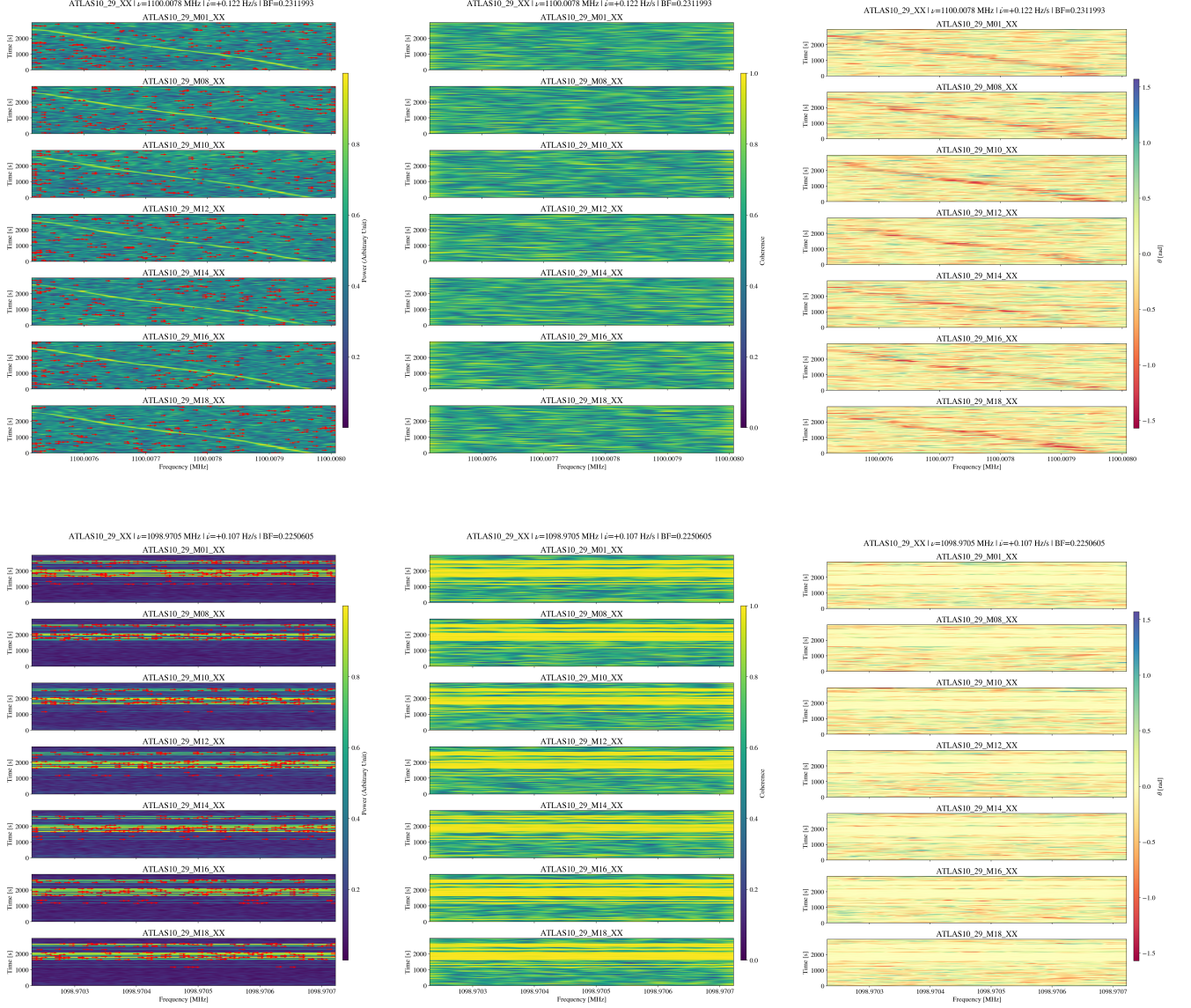


Figure 13. Waterfall plots (left), coherence map (middle) and orientation angle (right) for Doppler-drifting RFI signal (top) and relatively broadband RFI signal (bottom) appearing in all beams.

6. CONCLUSION

We perform ~ 4 –hr narrowband technosignature search toward 3I/ATLAS, the third confirmed ISO, with FAST L-band multibeam receiver in the frequency range of 1.05–1.45 GHz. The data was recorded on SETI backend with 7.5 Hz frequency resolution and 10 s sample time. We search for narrowband drifting signal with drift rates consistent with the relative motion of 3I/ATLAS and SNR threshold above 10, in four polarization channels.

The hit search is performed using `bliss` within $\pm 2 \text{ Hz s}^{-1}$. The obtained hits are filtered by HDBSCAN and expected drift rate. We apply Bayes factor to quantify the significance in the SNR differences between on-source and off-source. We also utilize structure tensor and PCA to featurize the morphology of the events.

After visual inspections, almost all potential candidates we obtain are obvious false positives and rejected as RFIs, except five chirp-up signals detected on 5 January 2026, which only appear in the central beam. These five chirp-up signals are finally rejected as instrumental RFIs instead of signal of interest, due to the consistency with the clock oscillator intermodulation in frequencies and inconsistency with the expected drift rate. Based on the null result, we can place a constraint no solid evidence for any narrowband transmitters with EIRP above $2.862 \times 10^{-3} \text{ W}$. We also propose a Bayesian model for the detection limit in transmitter occurrence probability and the transmitter power.

ACKNOWLEDGMENTS

We appreciate the staffs in FAST data center for approving our DDT application on FAST observing time. This work was supported by National Key R&D Program of China, No.2024YFA1611804 and the China Manned Space Program with grant No. CMS-CSST-2025-A01. This work made use of the data from FAST (Five-hundred-meter Aperture Spherical radio Telescope). FAST is a Chinese national mega-science facility, operated by National Astronomical Observatories, Chinese Academy of Sciences.

APPENDIX

A. EXPLAINED VARIANCE RATIO IN PCA FOR DRIFTING SIGNAL

Consider the dynamic spectrum $X_c \in \mathbb{R}^{N_t \times N_\nu}$. A narrow Doppler-drifting line can be idealized as a spectral profile,

$$X_c(t_i, \nu_j) \approx \alpha(t_i)g(\nu_j - \nu_0 - \dot{\nu}t_i), \quad (\text{A1})$$

where $\alpha(t_i)$ is the amplitude and $g(\nu)$ has characteristic width w_ν . For drifting regime $|\dot{\nu}|\tau_{\text{obs}} \gg w_\nu$, applying PCA to X_c is equivalent to diagonalizing the frequency-domain covariance,

$$C_\nu \equiv \frac{1}{N_t} X_c^\top X_c, \quad \text{EVR}_m = \frac{\lambda_m}{\sum_k \lambda_k}, \quad (\text{A2})$$

where $\{\lambda_m\}$ are the eigenvalues of C_ν (equivalently $\lambda_m = \sigma_m^2$, with σ_m the singular values of X_c). Substituting the drifting-profile yields

$$C_\nu(\nu_j, \nu_k) = \frac{1}{N_t} \sum_{i=1}^{N_t} \alpha^2(t_i)g(\nu_j - \nu_0 - \dot{\nu}t_i)g(\nu_k - \nu_0 - \dot{\nu}t_i). \quad (\text{A3})$$

When the drift spans many line widths, the correlation between channels depends primarily on the frequency separation $\Delta\nu = \nu_j - \nu_k$. Approximating $\alpha^2(t_i)$ by its time average $A^2 \equiv \langle \alpha^2 \rangle$ and replacing the discrete sum by an integral along the drift line gives an approximately shift-invariant kernel,

$$C_\nu(\nu_j, \nu_k) \approx K(\Delta\nu) = \frac{A^2}{|\dot{\nu}|\tau_{\text{obs}}} \int_{-\infty}^{\infty} g(u)g(u - \Delta\nu)du. \quad (\text{A4})$$

For a Gaussian line profile $g(\nu) \propto \exp[-\nu^2/(2w_\nu^2)]$, the correlation kernel is also Gaussian,

$$K(\Delta\nu) = K_0 \exp\left(-\frac{\Delta\nu^2}{4w_\nu^2}\right). \quad (\text{A5})$$

Over the drift span, define the number of frequency channels traversed as

$$N_{\text{span}} \equiv \text{round}\left(\frac{|\dot{\nu}|\tau_{\text{obs}}}{\delta\nu}\right), \quad (\text{A6})$$

and consider the discrete Fourier modes

$$v_m(j) = \exp\left(i\frac{2\pi mj}{N_{\text{span}}}\right), \quad m = 0, \dots, N_{\text{span}} - 1, \quad (\text{A7})$$

which approximately diagonalize a shift-invariant covariance. The corresponding eigenvalues can be written as the discrete Fourier transform of the sampled kernel $K_n \equiv K(n\delta\nu)$, For $|\dot{\nu}|\tau_{\text{obs}} \gg \delta\nu$ case,

$$\lambda_m = \sum_{n=0}^{N_{\text{span}}-1} K_n \exp\left(-i\frac{2\pi mn}{N_{\text{span}}}\right). \quad (\text{A8})$$

In the large-span limit, this sum is well-approximated by the continuous Fourier transform

$$\lambda_m \approx \int_{-\infty}^{\infty} K(\Delta\nu) e^{-ik_m \Delta\nu} d(\Delta\nu), \quad k_m \equiv \frac{2\pi m}{|\dot{\nu}|, \tau_{\text{obs}}}. \quad (\text{A9})$$

Using Equation (A5) and the Gaussian Fourier transform,

$$\int_{-\infty}^{\infty} \exp\left(-\frac{x^2}{4w_\nu^2}\right) e^{-ikx} dx = 2\sqrt{\pi}w_\nu \exp[-(kw_\nu)^2], \quad (\text{A10})$$

we obtain

$$\lambda_m \approx K_0(2\sqrt{\pi}w_\nu) \exp[-(k_m w_\nu)^2] = K_0(2\sqrt{\pi}w_\nu) \exp\left[-\left(\frac{2\pi m w_\nu}{|\dot{\nu}|\tau_{\text{obs}}}\right)^2\right]. \quad (\text{A11})$$

We define the EVR entropy as

$$H_{\text{EVR}} = -\sum_m p_m \ln p_m, \quad p_m = \frac{\lambda_m}{\sum_k \lambda_k}. \quad (\text{A12})$$

For $|\dot{\nu}|\tau_{\text{obs}} \gg w_\nu$, define

$$a \equiv \left(\frac{2\pi w_\nu}{|\dot{\nu}|\tau_{\text{obs}}}\right)^2 \ll 1. \quad (\text{A13})$$

Up to normalization, Equation (A11) implies $p_m \propto e^{-am^2}$, so that

$$p_m \approx \frac{e^{-am^2}}{\sum_k e^{-ak^2}} \approx \sqrt{\frac{a}{\pi}} e^{-am^2}, \quad (\text{A14})$$

where we have used the continuum approximation

$$\sum_k e^{-ak^2} \approx \int_{-\infty}^{\infty} e^{-ax^2} dx = \sqrt{\frac{\pi}{a}}. \quad (\text{A15})$$

Treating $p(x) = \sqrt{a/\pi} e^{-ax^2}$ as a continuous density yields

$$H_{\text{EVR}} \approx -\int_{-\infty}^{\infty} p(x) \ln p(x) dx = \frac{1}{2} \ln\left(\frac{\pi e}{a}\right) = \ln\left(\frac{|\dot{\nu}|\tau_{\text{obs}}}{2\pi w_\nu}\right) + \frac{1}{2} \ln(\pi e). \quad (\text{A16})$$

In addition, our derivation replaces the discrete modal sum and discrete Fourier transform by a continuous Gaussian integral and a continuous Fourier transform. For a finite drift span and a finite number of modes, this discrete-continuous approximation modifies the tail weights and induces spectral leakage in the discrete spectrum, which may increase H_{EVR} relative to the idealized expression.

B. CHIRP-UP DRIFTING POTENTIAL CANDIDATES

There are five potential candidates exhibit chirp-up drifting feature. Apart from the potential candidates with event ID 250, other four potential candidates listed in Table 4 are illustrated in Figure 14.

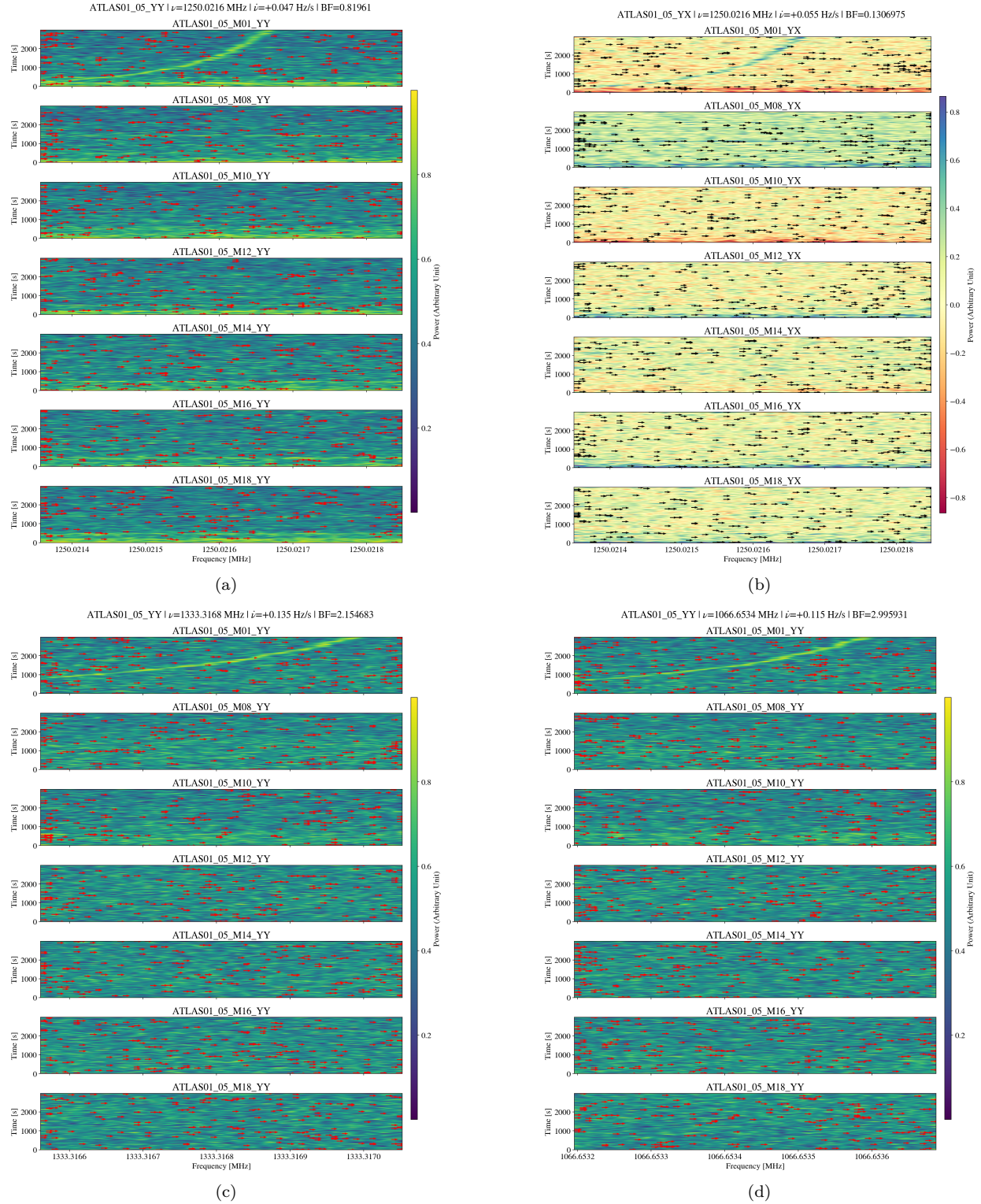


Figure 14. Four drifting potential candidates with similar chirp-up features with Figure 8. Panel (a) and (b) are actually the same signal in YY and YX channels, in spite of different drift rates given by `bliss`. Panel (c) and (d) are two chirp-up drifting signals with similar chirp-up morphological pattern different from the signals in Panel (a) and (b).

C. DERIVATIONS FOR BAYESIAN LIMITS

C.1. Posterior for Null Detection

For the ideal Gaussian noise in radio observation, the test statistic x satisfies $x \sim \mathcal{N}(\mu_0, \sigma^2)$ for pure noise. For the case of signal detection with EIRP of L , the mean of test statistic x becomes $m\mu_0 + \Delta\mu(L)$, then the SNR can be defined as

$$\text{SNR} = \frac{x - \mu_0}{\sigma_0}. \quad (\text{C17})$$

The SNR for pure noise satisfies $\text{SNR} | H_0 \sim \mathcal{N}(0, 1)$, while the SNR for signal detection should be $\text{SNR} | H_1 \sim \mathcal{N}(\Delta\mu(L)/\sigma_0, 1)$. The typical SNR for a signal $\mu_{\text{SNR}}(L) = \Delta\mu(L)/\sigma_0$ can be given by

$$\mu_{\text{SNR}}(L) = \frac{1}{\text{SEFD}} \sqrt{\frac{n_{\text{pol}}\tau_{\text{obs}}}{\delta\nu_{\text{ch}}}} \frac{L}{4\pi d^2} = cL \quad (\text{C18})$$

Then the probability \mathcal{P}_{det} of detecting a signal above SNR_{th} can be calculated by

$$\mathcal{P}_{\text{det}}(L) = \Pr(\text{SNR} > \text{SNR}_{\text{th}}) = 1 - \Phi(\text{SNR}_{\text{th}} - \mu_{\text{SNR}}(L)) = \Phi(cL - \text{SNR}_{\text{th}}). \quad (\text{C19})$$

We assume $T | p_T \sim \text{Bernoulli}(p_T)$, so that $\Pr(T = 1 | p_T) = p_T$ and $\Pr(T = 0 | p_T) = 1 - p_T$. Conditional on $T = 1$, the transmitter has an EIRP of L drawn from a prior $\pi(L)$, while for $T = 0$, L is not physically meaningful and will not enter the likelihood below. Consider K observational configurations, where configuration k contains N_k independent trials. For a given EIRP L , the single-trial detection probability in configuration k is $\mathcal{P}_{\text{det},k}(L)$. Using Bayes' theorem and assuming independent priors $\pi(p_T)$ and $\pi(L)$, the joint posterior for (p_T, L, T) is

$$p(p_T, L, T | \text{all0}) = \frac{\mathcal{L}(\text{all0} | T, L)\pi(L)\Pr(T | p_T)\pi(p_T)}{p(\text{all0})}, \quad (\text{C20})$$

where $\Pr(T | p_T) = p_T^T(1 - p_T)^{1-T}$, and the evidence is

$$p(\text{all0}) = \sum_{T \in \{0,1\}} \iint \mathcal{L}(\text{all0} | T, L)\pi(L)\Pr(T | p_T)\pi(p_T)dLdp_T. \quad (\text{C21})$$

Finally, we marginalize over the latent indicator T to obtain the posterior in (p_T, L) :

$$p(p_T, L | \text{all0}) = \sum_{T \in \{0,1\}} p(p_T, L, T | \text{all0}) \frac{[(1 - p_T)\mathcal{L}(\text{all0} | T = 0)] + [p_T\mathcal{L}(\text{all0} | T = 1, L)]}{p(\text{all0})} \pi(L)\pi(p_T). \quad (\text{C22})$$

Substituting Equations (34)-(35) gives a compact mixture-likelihood form:

$$p(p_T, L | \text{all0}) = \frac{\left[(1 - p_T) + p_T \prod_{k=1}^K (1 - \mathcal{P}_{\text{det},k}(L))^{N_k} \right] \pi(L)\pi(p_T)}{\iint \left[(1 - p_T) + p_T \prod_{k=1}^K (1 - \mathcal{P}_{\text{det},k}(L))^{N_k} \right] \pi(L)\pi(p_T)dLdp_T}. \quad (\text{C23})$$

C.2. Adopted Parameters and Hyperparameters

In this Appendix we summarize the prior families and the numerical hyperparameters adopted in the illustrative Bayesian analysis. These choices are intentionally simple and are not intended to represent a unique physical model. Rather, they encode conservative expectations that (i) the transmitter occurrence probability is small but poorly known in scale, and (ii) the EIRP may span orders of magnitude and is therefore more naturally parameterized in $\ln L$.

For the non-hierarchical models, We initially adopt a deliberately loose upper bound $p_{T,\text{max}} = 0.5$ to ensure that the prior support covers a broad range of plausible occurrence probabilities and parameterize $p_T = p_{T,\text{max}}q$. We consider (i) a scaled-beta prior $q \sim \text{Beta}(a, b)$ with $(a, b) = (5, 5000)$, which concentrates prior mass near $q \approx a/(a + b) \simeq 10^{-3}$ (thus $p_T \sim 5 \times 10^{-4}$) while retaining a long tail to larger values, and logit-normal mapping $p_T = p_{T,\text{max}} \text{sigmoid}(z)$ with $z \sim \mathcal{N}(\mu_p, \sigma_p^2)$ and $(\mu_p, \sigma_p) = (-3, 10)$, which is deliberately diffuse in logit space and therefore weakly informative for p_T over many orders of magnitude. For the EIRP we adopt a log-normal prior $\ln L \sim \mathcal{N}(\mu_L, \sigma_L^2)$ with $(\mu_L, \sigma_L) = (\ln 2, \ln 10)$, implying a median $L \simeq 2W$ and a multiplicative scatter of $\exp(\sigma_L) = 10$.

In the all-zero detection regime, the posterior mass concentrates well below this bound, with a characteristic scale $p_T \sim 5 \times 10^{-3}$ in non-hierarchical models. Therefore, we subsequently restrict the hierarchical analyses to a grid of smaller $p_{T,\max}$ values, $p_{T,\max} \in \{0.01, 0.008, 0.005\}$. For the scaled-beta hierarchical model we retain $p_T = p_{T,\max} q$ and use

$$q \mid m, \kappa \sim \text{Beta}(m\kappa, (1-m)\kappa), \quad m \sim \text{Beta}(\alpha_m, \beta_m), \quad \kappa \sim \text{Gamma}(a_\kappa, b_\kappa), \quad (\text{C24})$$

with $(\alpha_m, \beta_m) = (2, 2000)$ and $(a_\kappa, b_\kappa) = (5, 0.05)$. This places $m \sim 10^{-3}$, pushing the typical p_T to small values, while κ controls how tightly p_T is concentrated around m : larger κ produces stronger shrinkage (narrower posteriors in $\log p_T$) and makes the inferred (p_T, L) region more sensitive to the imposed upper bound $p_{T,\max}$.

For the logit-normal hierarchical model we adopt

$$z \mid \mu_p, \sigma_p \sim \mathcal{N}(\mu_p, \sigma_p^2), \quad p_T = p_{T,\max} \text{sigmoid}(z), \quad (\text{C25})$$

with $\mu_p \sim \mathcal{N}(\mu_{p,0}, \tau_{\mu_p}^2)$ and $\sigma_p \sim \text{HalfNormal}(s_{\sigma_p})$. We use $(\mu_{p,0}, \tau_{\mu_p}^2) = (-3, 4)$ and $s_{\sigma_p} = 2$, which yields a broad prior on p_T in logit space but still favors small p_T . Compared to the scaled-beta hierarchical model, this mapping tends to redistribute probability more smoothly in $\log p_T$, producing smaller morphological changes of the $\log p_T - \log L$ contours when $p_{T,\max}$ is varied.

For the EIRP hierarchical model we retain a log-normal form

$$\ln L \mid \mu_L, \sigma_L \sim \mathcal{N}(\mu_L, \sigma_L^2), \quad \mu_L \sim \mathcal{N}(\mu_{L,0}, \tau_{\mu_L}^2), \quad \ln \sigma_L \sim \mathcal{N}(\ln \sigma_{L,0}, \tau_{\ln \sigma_L}^2). \quad (\text{C26})$$

We adopt $(\mu_{L,0}, \tau_{\mu_L}^2) = (0, 1)$ and $(\ln \sigma_{L,0}, \tau_{\ln \sigma_L}^2) = (0.83, 0.25)$, corresponding to a prior median $L \sim 1\text{W}$ and a typical dispersion $\sigma_L \sim e^{0.83} \approx 2.3$.

In the all-zero detection regime, the likelihood provides limited leverage on p_T unless $\mathcal{P}_{\text{det}}(L)$ varies appreciably across the prior-supported range of L , hence $p_{T,\max}$ mainly controls the extent of the allowed region along $\log p_T$. As illustrative examples, we show the constraints for each parameter for scaled-beta and logit-normal p_T prior with $p_{T,\max} = 0.005$ in Figure 15. For intuition, EIRPs of 1-100 W are comparable to consumer electronics and small appliances. The analysis here uses these priors only as simple benchmarks to demonstrate how non-detections map into constraints on (p_T, L) .

REFERENCES

- Bolin, B., Abron, L.-M., Belyakov, M., et al. 2025a, The Astronomer’s Telegram, 17363, 1
- Bolin, B. T., Belyakov, M., Fremling, C., et al. 2025b, MNRAS, 542, L139, doi: [10.1093/mnras/542/l139](https://doi.org/10.1093/mnras/542/l139)
- Brzycki, B., Siemion, A. P. V., Pater, I. d., et al. 2022, AJ, 163, 222, doi: [10.3847/1538-3881/ac5e3d](https://doi.org/10.3847/1538-3881/ac5e3d)
- Campello, R. J. G. B., Moulavi, D., & Sander, J. 2013, in Advances in Knowledge Discovery and Data Mining, ed. J. Pei, V. S. Tseng, L. Cao, H. Motoda, & G. Xu (Berlin, Heidelberg: Springer Berlin Heidelberg), 160–172
- Chen, L.-F., Tsai, C.-W., Li, J.-Y., et al. 2024, Research in Astronomy and Astrophysics, 24, 105008, doi: [10.1088/1674-4527/ad7823](https://doi.org/10.1088/1674-4527/ad7823)
- Cocconi, G., & Morrison, P. 1959, Nature, 184, 844, doi: [10.1038/184844a0](https://doi.org/10.1038/184844a0)
- Cordiner, M. A., Roth, N. X., Kelley, M. S. P., et al. 2025, ApJL, 991, L43, doi: [10.3847/2041-8213/ae0647](https://doi.org/10.3847/2041-8213/ae0647)
- Enriquez, J. E., Siemion, A., Foster, G., et al. 2017, ApJ, 849, 104, doi: [10.3847/1538-4357/aa8d1b](https://doi.org/10.3847/1538-4357/aa8d1b)
- Eubanks, T. M., Hibberd, A., Bills, B. G., et al. 2025, Research Notes of the American Astronomical Society, 9, 329, doi: [10.3847/2515-5172/ae2915](https://doi.org/10.3847/2515-5172/ae2915)
- Farnham, T. L., Hood, M., Kelley, M. S. P., & Sunshine, J. M. 2025, Research Notes of the American Astronomical Society, 9, 266, doi: [10.3847/2515-5172/ae109f](https://doi.org/10.3847/2515-5172/ae109f)
- Huang, B.-L., Tao, Z.-Z., & Zhang, T.-J. 2023, AJ, 166, 245, doi: [10.3847/1538-3881/ad06b1](https://doi.org/10.3847/1538-3881/ad06b1)
- Huang, B.-L., Tao, Z.-Z., Zhang, T.-J., & Gajjar, V. 2026, AJ, 171, 51, doi: [10.3847/1538-3881/ae2470](https://doi.org/10.3847/1538-3881/ae2470)
- Jacobson-Bell, B., Croft, S., White, E., et al. 2025, Research Notes of the American Astronomical Society, 9, 351, doi: [10.3847/2515-5172/ae3083](https://doi.org/10.3847/2515-5172/ae3083)
- Jewitt, D., Hui, M.-T., Mutchler, M., Kim, Y., & Agarwal, J. 2025, ApJL, 990, L2, doi: [10.3847/2041-8213/adf8d8](https://doi.org/10.3847/2041-8213/adf8d8)
- Jiang, D., Qian, L., Guo, M., et al. 2025, arXiv e-prints, arXiv:2512.21969, doi: [10.48550/arXiv.2512.21969](https://doi.org/10.48550/arXiv.2512.21969)
- Jiang, P., Yue, Y., Gan, H., et al. 2019, Science China Physics, Mechanics, and Astronomy, 62, 959502, doi: [10.1007/s11433-018-9376-1](https://doi.org/10.1007/s11433-018-9376-1)

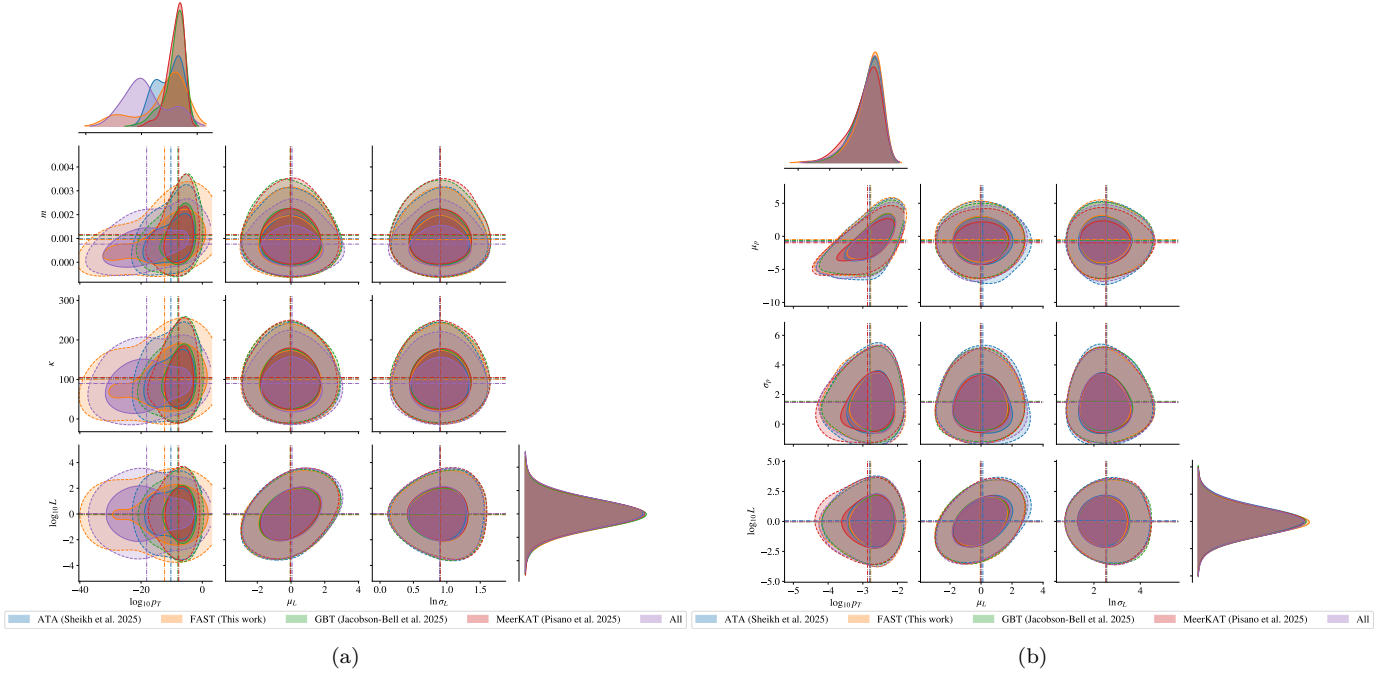


Figure 15. Posterior constraints for the scaled-beta (a) and logit-normal (b) p_T , with lognormal L hierarchical models under the all-zero detection. The contours show the joint posterior densities marginalized over nuisance parameters for the observing configurations in ATA, GBT, MeerKAT and this work. Solid and dashed curves enclose the 68% and 95% HPD regions, respectively. The top-left panel shows the 1-dimension marginal posterior of $\log_{10} p_T$, while the bottom-right panel shows the 1-dimension marginal posterior of $\log_{10} L$.

Jiang, P., Tang, N.-Y., Hou, L.-G., et al. 2020, *Research in Astronomy and Astrophysics*, 20, 064, doi: [10.1088/1674-4527/20/5/64](https://doi.org/10.1088/1674-4527/20/5/64)

Kareta, T., Champagne, C., McClure, L., et al. 2025, *ApJL*, 990, L65, doi: [10.3847/2041-8213/adfbdf](https://doi.org/10.3847/2041-8213/adfbdf)

Knutsson, H., Westin, C.-F., & Andersson, M. 2011, in *Lecture Notes in Computer Science*, Vol. 6688 (Springer Berlin Heidelberg), 545–556, doi: [10.1007/978-3-642-21227-7_51](https://doi.org/10.1007/978-3-642-21227-7_51)

Li, D., & Pan, Z. 2016, *Radio Science*, 51, 1060, doi: [10.1002/2015RS005877](https://doi.org/10.1002/2015RS005877)

Li, D., Gajjar, V., Wang, P., et al. 2020, *Research in Astronomy and Astrophysics*, 20, 078, doi: [10.1088/1674-4527/20/5/78](https://doi.org/10.1088/1674-4527/20/5/78)

Li, J.-K., Tao, Z.-Z., Wang, P., & Zhang, T.-J. 2026, *AJ*, 171, 78, doi: [10.3847/1538-3881/ae28cc](https://doi.org/10.3847/1538-3881/ae28cc)

Luan, X.-H., Huang, B.-L., Tao, Z.-Z., et al. 2025, *AJ*, 169, 217, doi: [10.3847/1538-3881/adbaef](https://doi.org/10.3847/1538-3881/adbaef)

Margot, J.-L., Pinchuk, P., Geil, R., et al. 2021, *AJ*, 161, 55, doi: [10.3847/1538-3881/abcc77](https://doi.org/10.3847/1538-3881/abcc77)

Nan, R., Li, D., Jin, C., et al. 2011, *International Journal of Modern Physics D*, 20, 989, doi: [10.1142/S0218271811019335](https://doi.org/10.1142/S0218271811019335)

Neukart, F. 2025, arXiv e-prints, arXiv:2511.07450, doi: [10.48550/arXiv.2511.07450](https://doi.org/10.48550/arXiv.2511.07450)

Opitom, C., Snodgrass, C., Jehin, E., et al. 2025, *MNRAS*, 544, L31, doi: [10.1093/mnras/slaf095](https://doi.org/10.1093/mnras/slaf095)

Pisano, D. J., Smirnov, O. M., Ivchenko, M., et al. 2025, *The Astronomer’s Telegram*, 17499, 1

Price, D., Enriquez, J., Chen, Y., & Siebert, M. 2019, *The Journal of Open Source Software*, 4, 1554, doi: [10.21105/joss.01554](https://doi.org/10.21105/joss.01554)

Qian, L., Yao, R., Sun, J., et al. 2020, *The Innovation*, 1, 100053, doi: [10.1016/j.xinn.2020.100053](https://doi.org/10.1016/j.xinn.2020.100053)

Santana-Ros, T., Ivanova, O., Mykhailova, S., et al. 2025, *A&A*, 702, L3, doi: [10.1051/0004-6361/202556717](https://doi.org/10.1051/0004-6361/202556717)

Seligman, D. Z., Micheli, M., Farnocchia, D., et al. 2025, *ApJL*, 989, L36, doi: [10.3847/2041-8213/adf49a](https://doi.org/10.3847/2041-8213/adf49a)

Sheikh, S. Z., Siemion, A., Enriquez, J. E., et al. 2020, *AJ*, 160, 29, doi: [10.3847/1538-3881/ab9361](https://doi.org/10.3847/1538-3881/ab9361)

Sheikh, S. Z., Garcia Lopez, V., Gerrard, I., et al. 2025, arXiv e-prints, arXiv:2512.18142, doi: [10.48550/arXiv.2512.18142](https://doi.org/10.48550/arXiv.2512.18142)

Smith, S., Price, D. C., Sheikh, S. Z., et al. 2021, *Nature Astronomy*, 5, 1148, doi: [10.1038/s41550-021-01479-w](https://doi.org/10.1038/s41550-021-01479-w)

Tao, Z.-Z., Huang, B.-L., Luan, X.-H., et al. 2023, *AJ*, 166, 190, doi: [10.3847/1538-3881/acfc1e](https://doi.org/10.3847/1538-3881/acfc1e)

Tao, Z.-Z., Zhao, H.-C., Zhang, T.-J., et al. 2022, *AJ*, 164, 160, doi: [10.3847/1538-3881/ac8bd5](https://doi.org/10.3847/1538-3881/ac8bd5)

- Tarter, J. 2001, *ARA&A*, 39, 511,
doi: [10.1146/annurev.astro.39.1.511](https://doi.org/10.1146/annurev.astro.39.1.511)
- Thompson, A. R., Moran, J. M., & Swenson, Jr., G. W.
2017, *Interferometry and Synthesis in Radio Astronomy*,
3rd Edition (Springer), doi: [10.1007/978-3-319-44431-4](https://doi.org/10.1007/978-3-319-44431-4)
- Traas, R., Croft, S., Gajjar, V., et al. 2021, *AJ*, 161, 286,
doi: [10.3847/1538-3881/abf649](https://doi.org/10.3847/1538-3881/abf649)
- Wang, Y., Zhang, H.-Y., Hu, H., et al. 2021, *Research in
Astronomy and Astrophysics*, 21, 018,
doi: [10.1088/1674-4527/21/1/18](https://doi.org/10.1088/1674-4527/21/1/18)
- Wilson, T. L., Rohlfs, K., & Hüttemeister, S. 2013, *Tools of
Radio Astronomy* (Springer),
doi: [10.1007/978-3-642-39950-3](https://doi.org/10.1007/978-3-642-39950-3)
- Zhang, J., Zhang, K., Grenfell, R., & Deakin, R. 2006,
Journal of Navigation, 59, 293,
doi: [10.1017/S0373463306003638](https://doi.org/10.1017/S0373463306003638)
- Zhang, Z.-S., Werthimer, D., Zhang, T.-J., et al. 2020, *ApJ*,
891, 174, doi: [10.3847/1538-4357/ab7376](https://doi.org/10.3847/1538-4357/ab7376)